eChem
https://www.sciltp.com/journals/eChem

Review

From Single-Site Regulation to Multi-Site Synergy: Recent Advances in Substitution Engineering of $Na_3V_2(PO_4)_3$ Cathodes for Sodium-Ion Batteries

Xia Liu †, Baolin Xie †, Zhenchao Bai, Rui Wang, Da Chen, Quan Zong, Qiaoling Kang * and Lijing Yan *

College of Materials and Chemistry, China Jiliang University, Hangzhou 310018, China
* Correspondence: kangqiaoling@cjlu.edu.cn (Q.K.); yanlijing@cjlu.edu.cn (L.Y.)
† These authors contributed equally to this work.

How To Cite: Liu, X.; Xie, B.; Bai, Z.; et al. From Single-Site Regulation to Multi-Site Synergy: Recent Advances in Substitution Engineering of $Na_3V_2(PO_4)_3$ Cathodes for Sodium-Ion Batteries. *eChem* **2026**, *2*(2), 9. https://doi.org/10.53941/echem.2026.100009

Received: 27 June 2026
Revised: 4 August 2026
Accepted: 6 August 2026
Published: 19 August 2026

Abstract: Sodium-ion batteries (SIBs) have emerged as one of the most promising alternatives to lithium-ion batteries for large-scale energy-storage applications owing to the natural abundance, low cost, and wide geographical distribution of sodium resources. Among various cathode candidates, $Na_3V_2(PO_4)_3$ (NVP) has attracted considerable attention because of its robust NASICON framework, high operating voltage, and excellent structural stability. Nevertheless, its intrinsically low electronic conductivity, limited reaction kinetics, and the high cost associated with vanadium resources continue to hinder practical applications. To address these challenges, extensive efforts have been devoted to site-specific substitution engineering of NVP-based cathodes. This review systematically summarizes recent advances in Na-site, V-site, and PO_4-site substitution strategies, as well as multi-site synergistic regulation approaches. The effects of different substitution mechanisms on crystal structure evolution, electronic configuration, Na^+ diffusion behavior, redox activity, and electrochemical performance are comprehensively discussed. Furthermore, the structure-property relationships governing various substitution strategies are critically analyzed and compared. Finally, the remaining challenges and future perspectives for rational compositional design, mechanistic understanding, and practical commercialization of NVP-based cathodes are highlighted. This review aims to provide valuable insights and design principles for the development of high-performance NASICON-type cathode materials for next-generation sodium-ion batteries.

Keywords: $Na_3V_2(PO_4)_3$; sodium-ion batteries; site-specific substitution; multi-site regulation; sodium storage mechanisms

1. Introduction

The growing demand for sustainable energy utilization has stimulated intensive research into advanced energy-storage technologies with higher efficiency and lower cost [1–9]. Beyond conventional lithium-ion batteries (LIBs), which currently dominate portable electronics and electric vehicles [10–14], a variety of alternative battery systems, including lithium-sulfur, sodium-ion, potassium-ion, and zinc-ion batteries, have attracted considerable attention. Among these candidates, sodium-ion batteries (SIBs) are regarded as one of the most promising options owing to the natural abundance and low cost of sodium resources [15–26], together with electrochemical characteristics comparable to those of lithium. Nevertheless, the relatively large ionic radius of Na^+ results in slow reaction kinetics and less favorable insertion/extraction behavior, which remain major obstacles

to further performance improvement. As a key component of SIBs, the cathode governs sodium-storage behavior and largely determines the attainable capacity, operating voltage, and energy density of the full cell. To date, the most extensively investigated cathode materials mainly include layered transition-metal oxides, polyanionic compounds, Prussian blue analogues, and sodium-containing organic compounds [27].

Among the various polyanionic cathodes investigated for sodium-ion batteries, $Na_3V_2(PO_4)_3$ (NVP) has attracted extensive attention owing to its NASICON-type framework [28–38], which provides three-dimensional Na^+ diffusion pathways and a theoretical capacity of 117.6 mAh g^{-1}. As illustrated in Figure 1a,b, both the number of publications and citation frequency related to NVP-based cathodes have increased markedly over the past decade, highlighting the growing research interest in this material system. Despite these advantages, the practical deployment of NVP remains constrained by its intrinsically low electronic conductivity and moderate energy density [39–44]. In addition, the relatively high cost of vanadium resources significantly increases the overall manufacturing expenses of vanadium-based batteries, thereby limiting their large-scale commercialization. Consequently, considerable efforts have been devoted to partially or completely replacing vanadium with more abundant and cost-effective transition-metal species. Nevertheless, single-site substitution at the V position often fails to fundamentally overcome the poor electronic transport associated with the insulating phosphate framework. Furthermore, the introduction of Jahn-Teller-active ions may induce transition-metal dissolution and local structural distortion during cycling, resulting in compromised structural integrity and electrochemical stability. These challenges underscore the necessity of developing more effective compositional engineering strategies for advanced NVP-based cathodes.

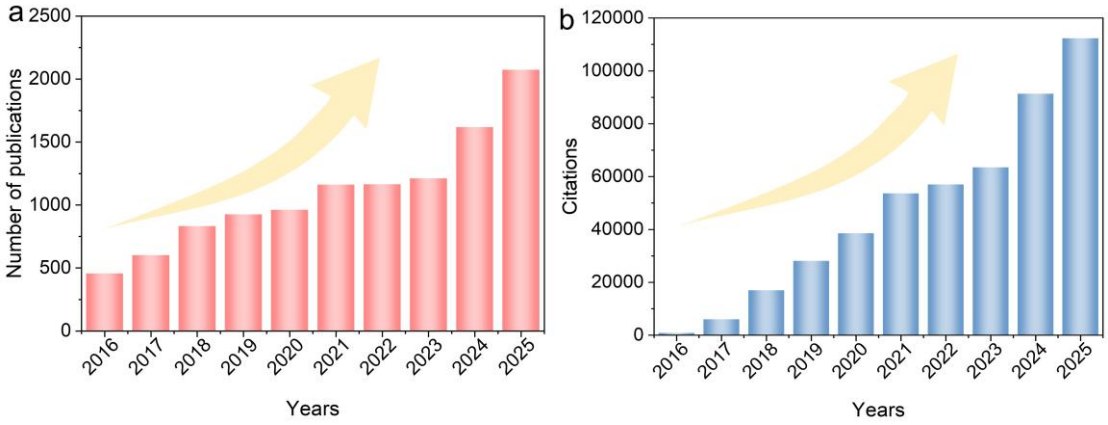

Figure 1. (**a**) Number of publications and (**b**) relevant citations from 2015 to 2025. Data were collected via Web of Science with the search keywords "Sodium-ion batteries" and "Sodium vanadyl phosphate", the retrieval date was 3 April 2026 and the images were generated by us based on the searched data.

With the rapid development of NVP-based cathodes [45–52], several review articles have been published to summarize recent advances in this field. Nevertheless, the majority of these studies have primarily concentrated on conventional modification strategies, including carbon coating, heteroatom incorporation, and morphology engineering [53–55]. Although these approaches have contributed significantly to improving electrochemical performance, a comprehensive understanding of site-specific substitution chemistry remains lacking. In particular, systematic discussions on the regulation of Na sites, V sites, and PO_4^{3-} polyanionic units, as well as their corresponding effects on crystal structure, electronic configuration, Na^+ transport behavior, and electrochemical properties, are still scarce. Therefore, a dedicated review focusing on the structure-property relationships associated with multi-site substitution is highly desirable for guiding the rational design of next-generation NVP-based cathode materials [56,57].

In view of these considerations, a comprehensive and critical review is required to elucidate the key modification strategies of $Na_3V_2(PO_4)_3$ and their underlying mechanisms for enhancing sodium-storage performance [58,59]. As illustrated in Figure 2, this review systematically summarizes the major approaches for tailoring NVP-based cathodes. First, Na-site engineering, including alkali-metal-ion substitution (e.g., Li^+ and K^+), is discussed with emphasis on its role in optimizing Na^+ diffusion pathways and accelerating reaction kinetics. Subsequently, V-site regulation, encompassing single-element doping, binary-element doping, medium-entropy and high-entropy engineering, as well as vanadium-free cathode design, is reviewed in terms of its effects on electronic conductivity, redox activity, and structural stability. In addition, anion-site modification through the partial substitution of PO_4^{3-} groups by species such as Si^{2-}, S^{2-}, MO^{4-} or F^- is examined for its ability to regulate

the local electronic environment and improve intrinsic charge-transport properties. Finally, multi-site engineering strategies, including Na/V co-substitution, Na/PO_4^{3-} co-substitution, V/PO_4^{3-} co-substitution, and triple-site regulation, are comparatively analyzed to reveal their synergistic effects and provide multidimensional design principles for the development of high-performance NVP cathodes. Finally, this review discusses the remaining challenges and future research priorities in NVP-based cathodes. By establishing the correlations between site-specific substitution strategies and electrochemical performance, it aims to provide fundamental design guidelines for the rational development of high-performance NVP materials. Particular emphasis is placed on identifying synergistic modification approaches that simultaneously enhance energy density [60], rate capability, cycling durability, and economic viability, thereby accelerating the practical deployment of sodium-ion batteries.

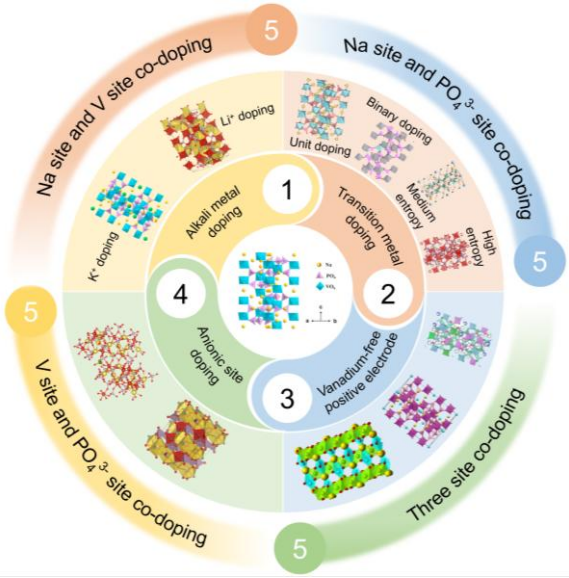

Figure 2. Schematic design of NVP-doped structures and their application in SIBs.

2. Alkali Metal Doping

$Na_3V_2(PO_4)_3$, as a representative of the NASICON type, lacks ideal electronic conductivity and ion diffusion ability, which is a defect that NVP needs to overcome urgently [61,62]. Alkali metal ion (e.g., Li^+, K^+) doping is an effective modification strategy to enhance the electrochemical performance of the materials by modulating the crystal structure of NVPs and optimizing the Na^+ transport channels. The core of alkali metal doping lies in the use of Li^+ or K^+ to partially replace the Na sites and change the lattice parameters and electronic structure of the material. Li^+ enhances the structural stability due to its small ionic radius (0.76 Å), while K^+ (1.38 Å) can widen the lattice spacing and promote the rapid migration of Na^+. In addition, alkali metal doping introduces additional redox active sites, which improves the specific capacity and cycle life of the material. In this section, the effects of Li^+ and K^+ doping on NVP materials will be systematically summarized and their potential applications in wide temperature region and high multiplicity conditions will be explored.

2.1. Li^+ Doping

The kernel mechanism of Li^+ doping NVP materials lies in its ability to displace Na sites and V sites in the crystal lattice of NVP owing to the suitable size and charge characteristics of Li^+. This stead transforms the electronic structure and Na^+ transport properties of the material remarkably.

For example, Cong et al. [63] synthesized $Li_xV_2(PO_4)_3$/C cathode materials for SIBs through hydrothermal assisted sol-gel method (Figure 3a). The cell volume decreases gradually with Li^+ increasing, which is consistent with the usual doping effect. Moreover, with the increase of Li^+ doping, Li^+ preferentially occupies the $Na_{(2)}$ site and then the $Na_{(1)}$ site (Figure 3b). At a Li^+ doping level of 0.2, the particle size of $Na_{2.8}Li_{0.2}V_2(PO_4)_3$/C reaches the maximum value (Figure 3c) and shows the best electrochemical performance. It achieved a reversible capacity of 116.9 mAh g^{-1} and maintained a capacity retention rate of 99.82% after 500 cycles. The result shows that the Li^+ doping significantly improves the diffusion coefficient of sodium ions, which enhances the reaction efficiency of the cathode material. In addition to the homovalent doping, in which Li^+ replaces Na^+, there are also studies of heterovalent substitution. For instance, Shen et al. [64] then substituted V^{3+} site in NVP anode materials by Li^+ to improve their sodium storage performance. It was found that this heterovalent ion substitution strategy not only

introduces electronic defects but also extends the migration path of sodium ions. In addition, the modified samples showed additional and particularly significant oxidation peaks at lower potentials (~3.2 V) (Figure 3d), which provided an effective suppression of electrochemical polarization. This phenomenon may be caused by the extraction of Na^+ at new sites derived from lattice defects in the optimized samples, indicating the rearrangement of Na^+ in the doped samples. The material provides outstanding low-temperature rate performance from 0.1 C to 5 C at −30 °C (Figure 3e), with the tremendous capacity retention of 90.2% after 3000 cycles at 55 °C (Figure 3f), proving its superb wide-temperature performance. This doping strategy optimizes the transport kinetics and electronic conductivity of sodium ions by modulating the lattice structure of the material.

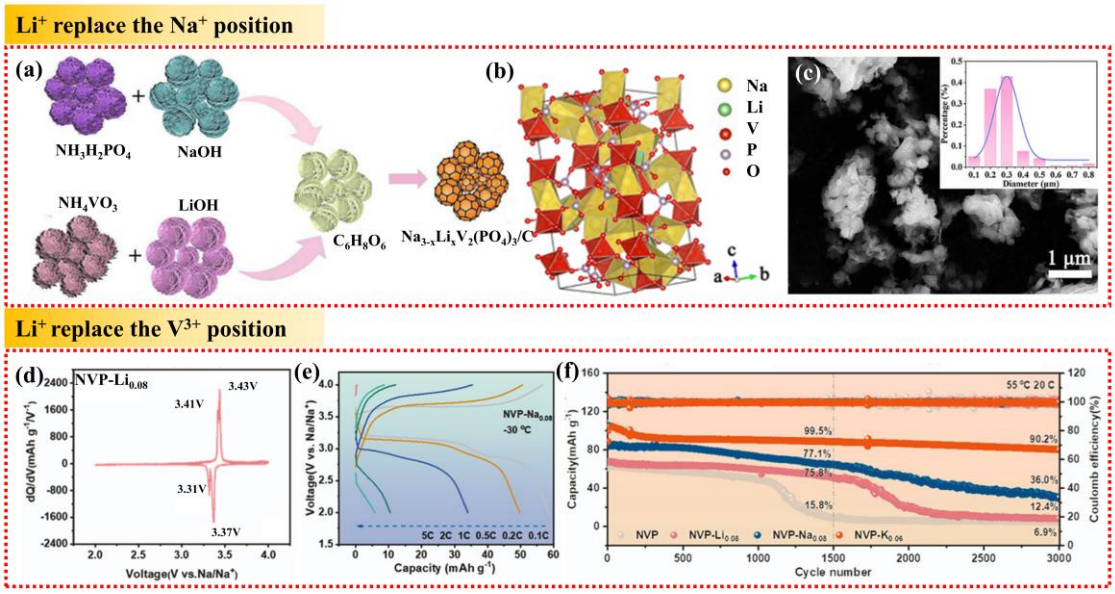

Figure 3. Examples of Li^+ doping: (**a**) The synthesis process flow chart of $Na_{3-x}Li_xV_2(PO_4)_3/C$, (**b**) The optimized crystal structure of $Na_{2.8}Li_{0.2}V_2(PO_4)_3$, (**c**) SEM images of $Na_{2.8}Li_{0.2}V_2(PO_4)_3/C$. Reproduced with permission from ref. [63]. Copyright 2024, Elsevier. (**d**) The dQ/dV curves of the initial cycle for NVP-$Li_{0.08}$, (**e**) Rate capabilities of NVP-$Na_{0.08}$ at −30 °C, (**f**) Cycling performance of as-synthesized cathodes. Reproduced with permission from ref. [64]. Copyright 2023, Elsevier.

Although Li^+ doping can effectively enhance the structural stability and Na^+ diffusion kinetics of NVP materials, its smaller ionic radius (0.76 Å) leads to lattice shrinkage, which may limit the further optimization of the Na^+ transport channel. Additionally, Li-doped materials still face the problem of capacity decay at high temperatures or extreme multiplicity conditions. Therefore, researchers have started to explore alkali metal doping strategies with larger ionic radii, among which potassium ion (K^+, 1.38 Å) have become a popular research topic due to its unique structure modulation.

2.2. K^+ Doping

K^+ doping into NVP is primarily implemented by rational design, which brings in K^+ without the host structure changing. This strategy could enlarge the crystal cell volume and widens the migration channels of Na^+, which is conducive to enhancing the reaction kinetics.

For example, Shen et al. [65] prepared $Na_{3-x}K_xV_2(PO_4)_3$ (x = 0, 0.05 and 0.10) via sol-gel method (Figure 4a). As the concentration of K^+ increases from 0 to 0.10 (the molar ratio of K^+/Na^+) in the NVP framework, an increase in the lattice parameters was found while the Na^+ (r_{Na+} = 1.02 Å) was replaced by the K^+ (r_{K+} = 1.38 Å) (Figure 4b). From Figure 4c, it can be clearly observed that K doped into the NVP material. Notably, NVP-$K_{0.05}$ delivers a discharge capacity of 100.1 mAh g^{-1} at 0.5 C and retains approximately 80% of its initial capacity after 1000 cycles at 10C (Figure 4d). Through rational design, the incorporation of K^+ into the NVP framework expands the unit cell volume and broadens the Na^+ migration channels, which ultimately advances the electrochemical performance. Same as Li^+ doping, K^+ can not only replace Na^+, but also replace V to reduce the impact of V on the environment. Shen et al. [64] reported that K^+ substitution for V^{3+} achieves lattice modulation, contributing the generation of electronic defects and widening the migration pathway for Na^+ (Figure 4e). For the K^+ substituted cathode, the capacitance retention at 0.2 C was 96.9% after 200 cycles under −30 °C, and a discharge capacity of 127.8 mAh g^{-1} at 0.1 C was achieved under 55 °C. To further understand the phase structure evolution of NVP-$K_{0.06}$ during charging and

discharging, in-situ XRD experiments were performed (Figure 4g). The diffraction peaks of (104), (113), (024), (116), (300), and (221) shift to higher angle during charging and reverse back to the original position during discharging, illustrating a highly reversible phase transition in the initial cycle. The splitting of the (104) peak followed by the disappearance/reappearance of (211/116) represents the two-phase reaction mechanism involved in the charging and discharging process, proving high reversibility and a low lattice volume change of 0.82%. In this regard, the first and third stages exhibit solid-solution reaction characteristics, while the second stage shows a two-phase reaction range.

The core advantage of K^+ doping is its large ionic radius (1.38 Å), which can effectively expand the cell volume of NVP and broaden the migration channels of Na^+, thus significantly enhancing the migration kinetics of Na^+. However, there are still some shortcomings. First and for most, K^+ doping may lead to significant changes in lattice parameters, which in turn affects the structural stability of the materials. At high temperatures or extreme multiplicity conditions, such structural changes may lead to capacity decay. Secondly, K^+ doping may introduce additional impurity phases, such as potassium by-products, which may adversely affect the electrochemical performance of the electrode materials. Future work may aim to develop and optimize more efficient doping schemes to overcome the structural side effects of K^+ doing.

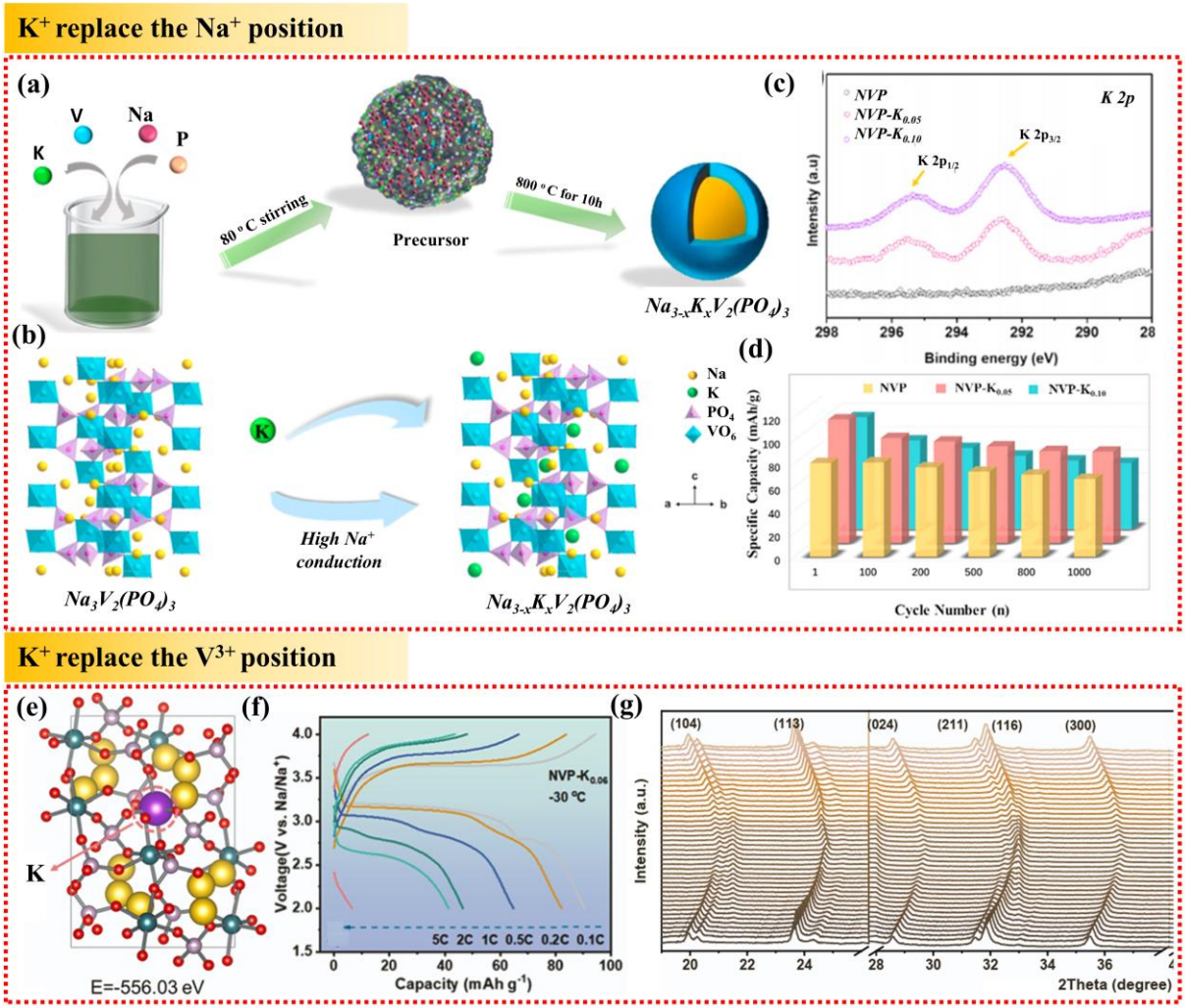

Figure 4. Examples of K^+ doping: (**a**) The synthetic route of $Na_{3-x}K_xV_2(PO_4)_3$ materials, (**b**) The schematic illustration of the structural stabilization of NVP electrode materials by doping K^+ into the Na^+ sites, (**c**) X-ray photoelectron spectroscopy obtained from the $Na_{3-x}K_xV_2(PO_4)_3$ collected in the K 2p regions, (**d**) Cycling performance of the samples at 10 C. Reproduced with permission from ref. [65]. Copyright 2023, Elsevier. (**e**) Schematic diagrams of the optimized crystal structure of NVP-K cathodes, (**f**) Rate capabilities of NVP-$K_{0.06}$ at −30 °C, (**g**) In-situ XRD patterns at a current rate of 0.1 C. Reproduced with permission from ref. [64]. Copyright 2023, Elsevier.

Alkali metal doping is an effective strategy to optimize the electrochemical properties of NVP cathode materials (Table 1). For example, Li^+ doping reduces Na^+ site vacancies, suppresses lattice distortion, and improves

cycling stability. K^+ doping reduces the Na^+ migration energy barrier by enlarging the cell volume. However, alkali metal doping still has some limitations, such as capacity decay at high multiplicity and structural instability under high temperature conditions. Future studies can combine composite modification strategies to further enhance the comprehensive performance of the materials. Overall, alkali metal doping provides an important technical path for the commercial application of NVP materials, but more in-depth exploration on material design and preparation process is still needed.

Table 1. the summary of the characteristics of alkali metal doping.

Doping Type		Characteristic	Materials	Rate Capability [mAh g^{-1}]	Cyclic Stability [mAh g^{-1}/Cycle]	Ref.
Alkali metal doping	Li doping	Li^+ can activate the Na sites and increase the specific capacity. However, the small size of Li^+ may lead to local stress changes in the crystal structure during charging and discharging, affecting the long-term cycling stability of the material.	$Na_{2.8}Li_{0.2}V_2(PO_4)_3$/C	102.0 (20 C)	89.76% (500)	[63]
			$Na_3V_{1.92}Li_{0.08}(PO_4)_3$	119.8 (0.1 C)	85.3% (20 C/3000)	[64]
	K doping	The larger ionic radius of K^+ is used to partially replace the Na^+, which could increase the lattice volume of NVP, providing a wider channel for Na diffusion. However, K^+ themselves do not participate in electrochemical reactions, which may reduce the theoretical specific capacity of the material to some extent.	NVP-$K_{0.05}$	100.1 (0.5 C)	79.96% (10 C/1000)	[65]
			NVP-$K_{0.06}$	128.8 (0.1 C)	99.1% (20 C/3000)	[64]

3. Transition Metal Doping

NVP has the advantages of high voltage plateau, high theoretical specific capacity, and stable crystal structure, but its low intrinsic electronic conductivity limits its commercial application. Transition metal cation doping of NVP is an effective modification method to partially or completely replace V with relatively inexpensive and nontoxic metal elements [66–68], resulting in the formation of new NASICON-type phosphates. Doping with transition metal cations (e.g., Fe, Ni, Mn, Cr, Ti, etc.) synergistically enhance the electronic conductivity [69,70], crystal structure stability and Na^+ diffusion rate, enhancing the specific capacity, cycling stability and high-rate performance. In general, transition metal cation doping of NVPs includes two strategies: unit doping and multi-doping. The two doping methods have their own advantages. The application potential of NVPs in the field of energy storage can be significantly enhanced through a reasonable choice of doping strategy.

3.1. Unit Doping

Unitary doping refers to the doping of NVP using only one transition metal cation such as the Fe, Mn, Cr, Ti, etc. to replace V. Its preparation process is simple, easy to control the doping concentration and homogeneity, and can be optimized for specific properties such as electrical conductivity or structural stability. For example, Fe doping can improve electronic conductivity and cyclic stability, while Ti doping can enhance structural stability and Na^+ diffusion rate.

3.1.1. Doping Mn

The Mn based NASICON-type material obtained by replacing the V part of $Na_3V_2(PO_4)_3$ structure with Mn element has two major advantages, one is the high energy density and another is high cost-effectiveness. Thereinto, Mn based NASICON materials can undergo multiple electron transfer reactions of Mn^{2+}/Mn^{3+} and Mn^{3+}/Mn^{4+} during electrochemical reactions, providing high theoretical specific capacity and operating voltage [71–74].

For example, Zhao et al. [75] prepared a series of carbon coated $Na_{3.75}Mn_{0.75}V_{1.25}(PO_4)_3$ (NMVP/xVitC, x = 1, 2, 3) cathode materials using vitamin C (VitC) as a carbon source via a sol-gel method (Figure 5a). The average discharge capacity of NMVP/2VitC is 105.6, 100.1, 97.8, 95.7, 92.9, and 89.8 mAh g^{-1} at 0.2, 0.5, 1, 2, 5, and 10 C, respectively, which shows excellent rate capability (Figure 5b). The volume contraction is about 8.8% due to the extraction of Na^+ from $Na_{3.75}Mn_{0.75}V_{1.25}(PO_4)_3$. After discharging to 2.5 V, all diffraction peaks return to their original positions. The lattice constants are similar to the original values, indicating a high structural reversibility of NMVP/2VitC in the Na^+ abstraction process (Figure 5c). It confirmed that the incorporation of Mn into the NMVP/2VitC cathode serves multiple critical functions. First, Mn introduces an additional Mn^{2+}/Mn^{3+} redox couple, which contributes to the specific capacity and increases the average working voltage (Figure 5d). Second, partial substitution of V with earth-abundant Mn significantly reduces material cost and toxicity, making the cathode more suitable for large-scale energy storage. Third, the larger ionic radius of Mn^{2+} (0.82 Å) compared to

V^{3+} (0.64 Å) expands the lattice parameter *a*, thereby enlarging the Na^+ diffusion channels and optimizing the bottleneck size for faster sodium-ion transport. Overall, the Mn element plays an indispensable role in balancing high electrochemical performance, structural reversibility, and low cost in this NASICON-type cathode.

In addition to the sol-gel method, Chen et al. [76] used a conventional high-temperature solid-state reaction to prepare $Na_3V_{1.5}Mn_{0.5}(PO_4)_3$ (NVP-Mn(0.5)) cathodes. The introduction of Mn^{3+} into the NVP-Mn(0.5) cathode plays a critical role in activating a reversible three-electron reaction, thereby significantly boosting the energy density. Specifically, Mn^{3+} doping successfully activates the high-potential V^{4+}/V^{5+} redox couple at ~3.9 V, in addition to the existing V^{2+}/V^{3+} and V^{3+}/V^{4+} couples, enabling three electrons to participate in the electrochemical process within an extended voltage window of 1.4–4.0 V (Figure 5e). Ex-situ XRD further reveals a combined single-phase and bi-phase sodium storage mechanism, demonstrating excellent structural reversibility (Figure 5f). As shown in Figure 5g, NVP-Mn(0.5) provides a first discharge capacity of up to 170.9 mAh g^{-1} at 0.5 C, demonstrating that the three-electron redox reaction was fully realized after Mn^{3+} doping. Bader charge and electron localization function (ELF) analyses indicate that Mn^{3+} substitution strengthens the Mn-O and P-O bonds, enhancing the structural stability of the NASICON framework (Figure 5h).

In a word, after introducing the Mn^{3+}, the band gap significantly decreased, which improves the intrinsic electronic conductivity of NVP and activates the high potential V^{4+}/V^{5+} redox pairs successfully.

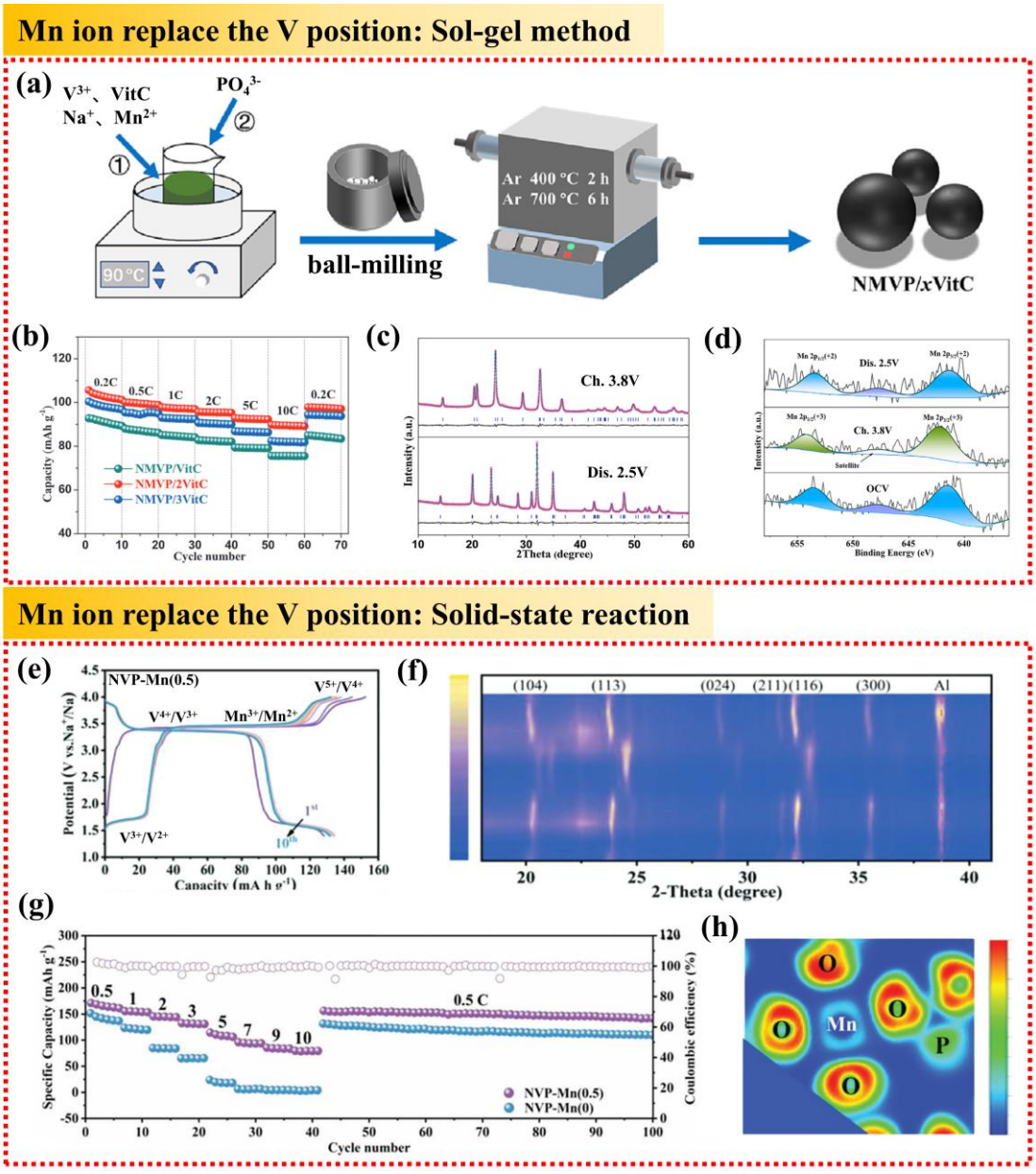

Figure 5. Examples of Mn ion doping: (**a**) Schematic of the preparation procedure of NMVP/xVitC composites, (**b**) Rate performances from 0.2 to 10 C, (**c**) Rietveld refinement of NMVP/2VitC, (**d**) XPS spectra of Mn 2p. Reproduced with permission from ref. [75]. Copyright 2023, Elsevier. (**e**) Charge/discharge curves for the initial ten cycles of NVP-

Mn(0.5), (**f**) 2D contour plots of ex-situ XRD patterns of NVP-Mn(0.5) in different charge and discharge states, (**g**) Rate performance, (**h**) ELF maps of NVP-Mn (0.5). Reproduced with permission from ref. [76]. Copyright 2023, Wiley.

3.1.2. Doping Fe

Fe doping modulation serves as an effective strategy for improving the electrochemical properties, primarily through the substitution of V^{3+} sites in the NASICON framework. By modulating the ratio of Na, Fe and V, the obtained Fe-based NASICON type materials exhibit great electronic conductivity and can activate multi-electron redox reactions, which ultimately results in a notably high energy density in SIBs.

For example, Zhou et al. [77] synthesized NASICON-type $Na_{3+x}V_{2-x}Fe_x(PO_4)_3$ cathode materials via a one-step solid-phase method, in which V was partially replaced by high-abundance and low-cost Fe (Figure 6a). In addition, the binding of divalent and trivalent Fe can occur simultaneously, suggesting the coexistence of slight oxidation and mixed valence of Fe in the NVFP material (Figure 6b). The unpaired electrons in the 3d orbitals of Fe are inseparable from the redox activation of the high valence state. Combined NVFP with a hard carbon (HC) anode (Figure 6c), the HC//NVFP full cell exhibits high-rate performance and long cycle life (3000 stable cycles at 50 C) (Figure 6d). This outstanding performance is primarily due to the incorporating of Fe also alters the arrangement of Na^+ sites within the structure, promoting preferential occupancy of the active Na2 sites by Na^+, which in turn supplies available active Na^+ for the V^{4+}/V^{5+} redox process.

In addition, our research group [78] fabricated carbon-coated $Na_3V_{1.7}Fe_{0.3}(PO_4)_3$ (NVFP) through sol-gel and thermal reduction routes with low-cost Fe^{3+} as substitution dopant. In-situ XRD contour plots (Figure 6e) exhibit symmetric and continuous migration of diffraction peaks during sodiation, which originates from Fe^{3+}-mediated activation of latent V^{4+}/V^{5+} redox pairs and guarantees highly reversible lattice evolution. The rate performance curves (Figure 6f) clearly verify that NVFP delivers much higher discharge capacities at all tested current densities compared with pure NVP, showing prominent rapid sodium storage capability. The schematic crystal regulation mechanism (Figure 6g) further illustrates that Fe substitution introduces abundant oxygen vacancies, shortens Na^+ migration paths and accelerates electron transport simultaneously. Besides lowering vanadium usage and material cost, Fe-doped NVFP can provide sufficient sodium reserves in full-cell systems to compensate irreversible Na loss consumed by SEI film formation, and the activated high-voltage V^{4+}/V^{5+} redox reaction greatly elevates the overall energy density relative to bare NVP.

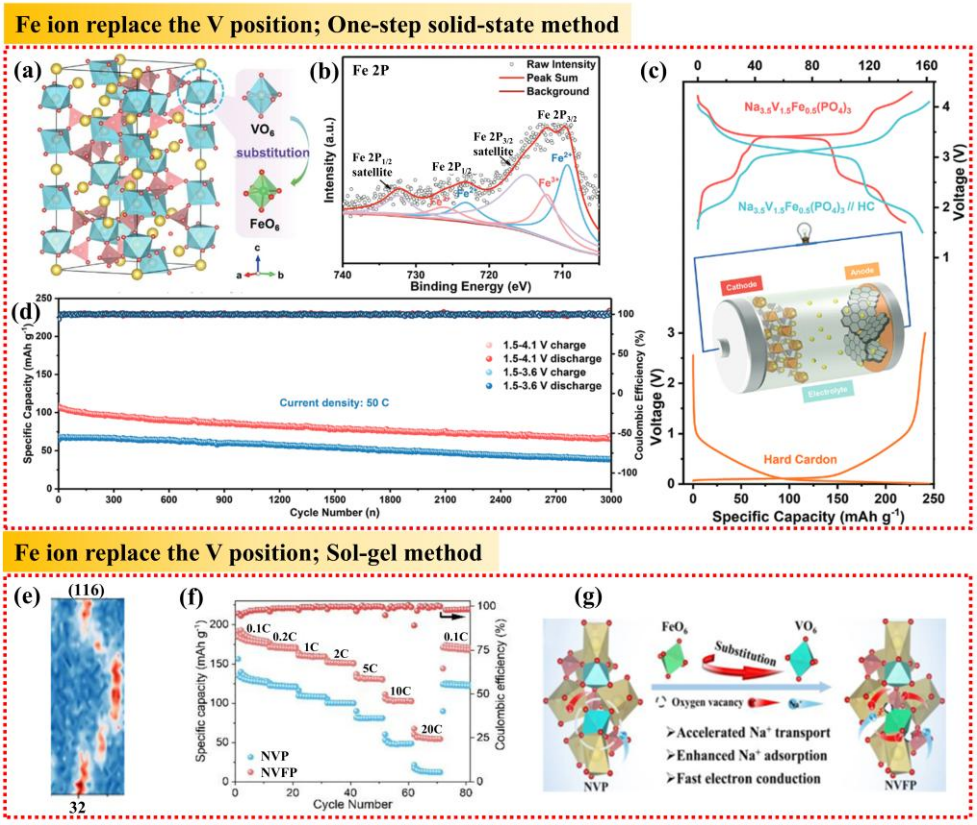

Figure 6. Examples of Fe ion doping: (**a**) Schematic illustration of the crystal structure of the NASICON-type $Na_{3+x}V_{2-x}Fe_x(PO_4)_3$ materials, (**b**) High-resolution Fe 2p XPS spectra, (**c**) Charge-discharge profiles of NVFP

cathode, HC anode and HC//NVFP full cells and schematic illustration of full cells (inset), (**d**) Long-term cycling stability at 50 C. Reproduced with permission from ref. [77]. Copyright 2023, Wiley. (**e**) The operando XRD contour map of NVFP electrode collected at selected angle range. (**f**) The rate performance comparison of different electrodes. (**g**) Schematic diagrams showing the crystal structures and superiorities of NVP and NVFP. Reproduced with permission from ref. [78]. Copyright 2025, Elsevier.

In summary, the doping of Fe can activate the high-voltage V^{4+}/V^{5+} redox pair, enabling multi-electron reactions and significantly enhancing the energy density. On the other hand, by utilizing the capacity of the low-voltage plateau of Fe^{2+}/Fe^{3+}, the irreversible loss of Na^+ caused by the formation of the SEI film in the entire battery can be compensated to solve the irreversible capacity loss of the entire battery. In addition, the occupancy of Na^+ at the Na2 site can be adjusted, which reduces the migration energy barrier and enhances the electronic conductivity.

3.1.3. Doping Cr

The Cr ion usually takes the place of V in the NVP due to the similar ionic radius and valence states of Cr and V. In addition, Cr doping can modulate the redox potential of V, decreasing V^{2+}/V^{3+}, V^{3+}/V^{4+} and V^{4+}/V^{5+} between the potential gaps. This moderating effect makes it easier to activate the three-electron reaction of V, thus increasing the specific capacity and energy density of the material.

For instance, Jian et al. [32] synthesized Cr-substituted $Na_3V_{1.3}Cr_{0.7}(PO_4)_3$@C ($NV_{1.3}Cr_{0.7}P$) cathode with a nanoparticle structure for SIBs using a simple sol-gel method (Figure 7a). Thanks to the advantages brought by Cr doping and nanostructures, the $NV_{1.3}Cr_{0.7}P$ exhibits excellent cycling stability, retaining 74.8% of its capacity after 5000 cycles at a current density of 5 A g^{-1}, and an excellent multiplication performance of 79.2% at 10 A g^{-1}. This is because Cr substitution lowers the diffusion energy barrier for Na^+, thereby boosting smoother Na^+ insertion and extraction processes. Furthermore, after Cr substitution, the energy level from Cr is introduced near the Fermi level in $NV_{1.3}Cr_{0.7}P$ with a reduced band gap to 0.080 eV, which significantly improves the electrical conductivity of $NV_{1.3}Cr_{0.7}P$ (Figure 7b). Compared with the nanoparticle structure, the hollow microsphere structure can effectively increase the sodium storage sites. For example, Mai and his colleagues [79] synthesized a Cr-doped $Na_3V_{4/3}Cr_{2/3}(PO_4)_3$@C (NVCP@C) with hollow sphere structure by spray drying method (Figure 7d). The electronic structure can be optimized by Cr^{3+}, which can induce the voltage platforms of $V^{5+}/^{4+}$, $V^{4+}/^{3+}$, and $V^{3+}/^{2+}$ in the window of 1.5–4.4 V. The NVCP@C achieves an excellent cycling stability with 86% capacity retention at 5 A g^{-1} for 2000 cycles (Figure 7e). Moreover, the changes in the polyanionic framework of NVCP@C is reversible accompanying by solid-solution reaction and two-phase reaction mechanisms co-exist during charge/discharge processes during the charge/discharge cycle, which are induced by the Na^+ insertion/extraction (Figure 7f).

In conclusion, the substitution of Cr for V not only activates the V^{2+}/V^{3+} and V^{4+}/V^{5+} redox pairs, enabling nearly a 3-electron transfer. Moreover, the intense two-phase reaction can be transformed into a continuous solid solution reaction with volume changes. Secondly, it can significantly reduce the band gap and lower the migration energy barrier for Na^+.

3.1.4. Doping of Other Elements

In addition to common elements like Fe, Mn and Cr, studies have found that many other cations with different valence states could be used to substitute the V site for single transition metal doping in NVP. This substitution strategy is also designed to regulate the crystal structure and improve the intrinsic electronic conductivity, including Al, Ti, Ga, etc.

For instance, Sun et al. [80] prepared $Na_3V_{1.5}Al_{0.5}(PO_4)_3$ by sol-gel method. Thereinto, the Al^{3+} substitution improves the covalency, phase structure stability and electrical conductivity of the NASICON framework, which give evidence for the structural stability and the excellent room-temperature and low-temperature cycling performance (Figure 8a). Furthermore, compared to NVP, $Na_3V_{1.5}Al_{0.5}(PO_4)_3$ proves an additional Al 2p orbital excluding Na 3s, V 3d, O 1s, and P 2p hybridized orbitals. Notably, due to the hybridized Al 2p orbital, the forbidden bandwidth of $Na_3V_{1.5}Al_{0.5}(PO_4)_3$ (1.505 eV) is smaller than that of NVP (2.406 eV), suggesting that the Al^{3+} substitution induces an enhancement of the electron and Na^+ charge transfer capacity (Figure 8b). As a result, the $Na_3V_{1.5}Al_{0.5}(PO_4)_3$ shows a high reversible capacity of 163 mAh g^{-1} by reducing V^{2+} to V^{5+} via a three-electron redox reaction (Figure 8c). In addition, Zhu et al. [81] prepared a series of NASICON-type cathode materials ($Na_{3-x}V_{2-x}Ti_x(PO_4)_3$/C, x = 0, 0.5, 1) by systematically adjusting the V-Ti ratio through spray-drying-assisted annealing. Thereinto, NVTP-0.5 is assembled from a large number of tightly packed nanoparticles, and the surface appears relatively rough and seamless, which can effectively avoid deformation or crushing (Figure 8d). The in-

situ XRD characterization also indicates the formation of new phase features typical of two-phase reactions during charge process. And the diffraction peaks shift back to their original positions in an almost symmetrical manner during the discharge process, indicating that a significant reversible phase transition occurred throughout the cycling process (Figure 8e). The high stability of Ti helps to reduce the forbidden bandwidth and increase the ionic and electronic conductivities, resulting in excellent electrochemical properties. As a result, the assembled HC//NVTP-0.5 full cell also provides an initial capacity of 150.0 mAh g^{-1} and an average output voltage of 2.67 V at 10 mA g^{-1}, achieving a high energy density of 400 Wh kg^{-1} (Figure 8f). Moreover, the rare earth element Ga^{3+} is frequently considered as a good dopant to enhance the structural stability. Chen et al. [82] synthesized $Na_3V_{2-x}Ga_x(PO_4)_3$ cathodes (NVP-$Ga_{0.75}$) via a common high temperature solid phase reaction method. It indicated that the partial substitution of Ga^{3+} for V^{3+} results in the activation of three redox pairs (V^{2+}/V^{3+}, V^{3+}/V^{4+}, and V^{4+}/V^{5+}), suggesting multi-electrons (>2e^-) involved in the reversible reaction, and simultaneously the electronic conductivity of the materials is effectively enhanced (Figure 8g). In addition, the Na^+ diffusion coefficient (D_{Na^+}) of NVP-Ga0.75 is higher than that of NVP-Ga0, which contributes to the rate per unit volume (Figure 8h). As a result, the NVP-Ga 0.75 has excellent performance, presenting a reversible capacity of 152.3 mAh g^{-1} (497.6 Wh kg^{-1}) and a capacity retention of 90% after 70 cycles at 1 C (Figure 8i).

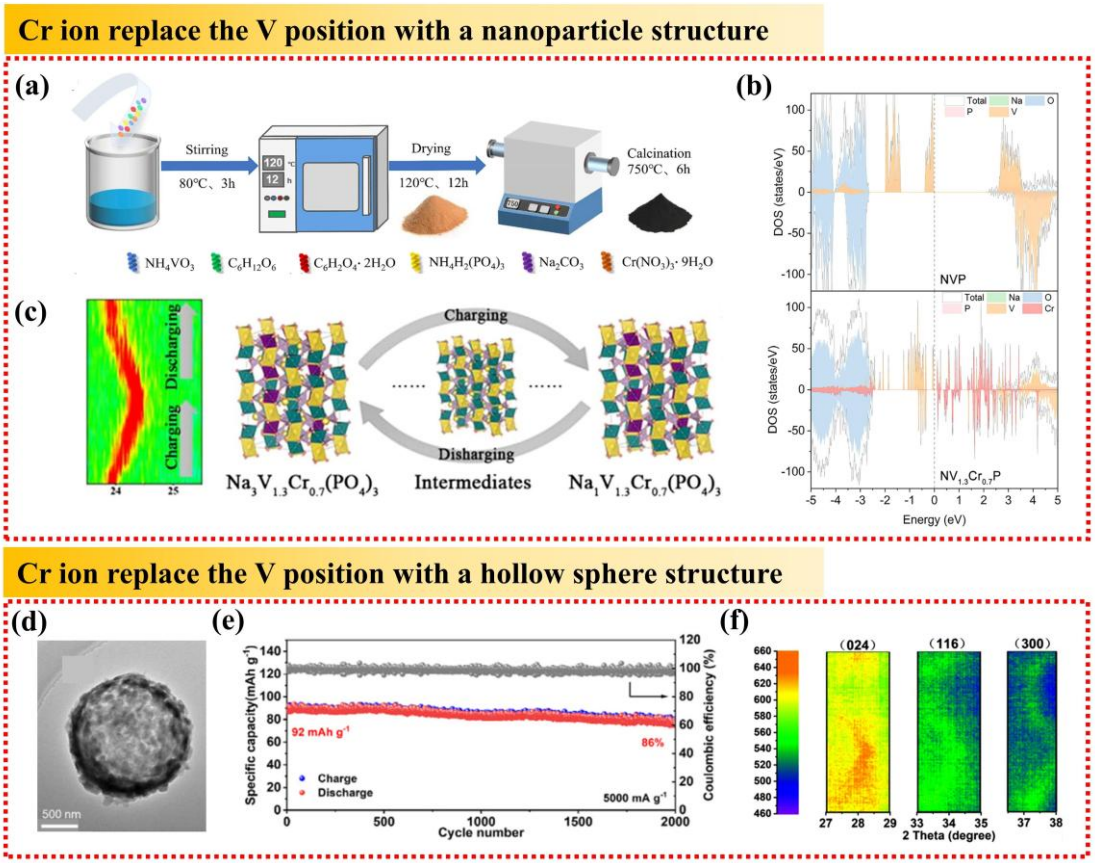

Figure 7. Examples of Cr ion doping: (**a**) Schematic diagram of the sol-gel synthesis process of $NV_{1.3}Cr_{0.7}P$. (**b**) The density of states of NVP and $NV_{1.3}Cr_{0.7}P$ structures. (**c**) Conversion mechanism diagram of $NV_{1.3}Cr_{0.7}P$. Reproduced with permission from ref. [32]. Copyright 2025, Elsevier. (**d**) SEM image of NVCP@C, (**e**) Coulombic efficiency and cycling performance at 5000 mA g^{-1} of NVCP@C. (**f**) In-situ XRD patterns of NVCP@C. Reproduced with permission from ref. [79]. Copyright 2023, Elsevier.

In a word, partially substituting electrochemically inactive ions with Al, Ti, or Ga can significantly improve the crystal structure and electrochemical properties of NVP materials. The high-potential V^{4+}/V^{5+} redox couple is successfully activated, enabling multi-electron reactions. Meanwhile, structural stability and electronic/ionic conductivity are enhanced, resulting in NASICON-type cathode materials with high energy density, long cycle life, and wide-temperature-range adaptability.

In summary, transition metal single site doping including Fe, Ni, Mn, Cr, Ti, etc. significantly optimizes the NVP's crystal structure, improves electronic conductivity and accelerates Na^+ diffusion rate, which are leading to higher specific capacity, excellent multiplicity and long cycle stability. However, single doping often faces the problem of limited performance enhancement and difficulty in accommodating multiple performance requirements.

In contrast, multi-element doping (including binary, medium-entropy and high-entropy doping) further improves the structural integrity and cycling stability of materials by integrating the advantages of multiple elements, providing a new idea for the development of high-performance NASICON-type cathode materials.

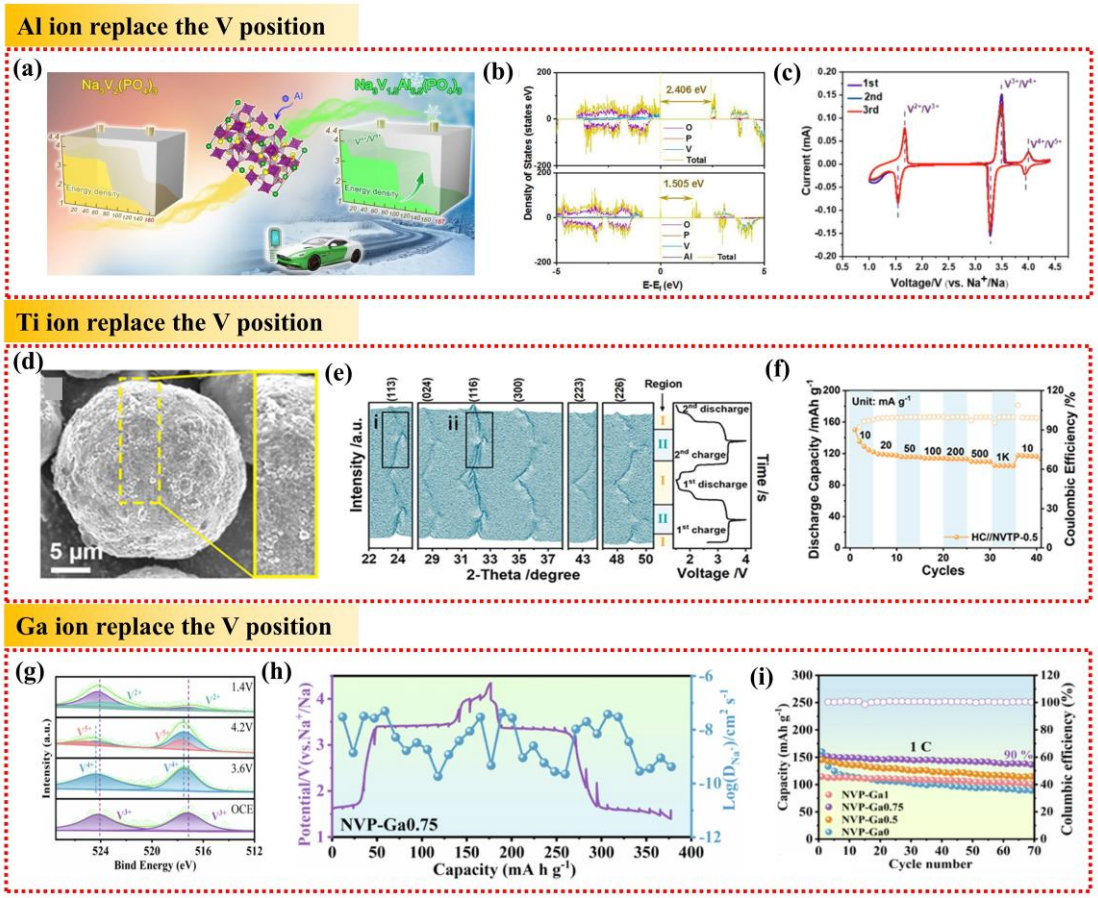

Figure 8. Examples of other elements doping: (**a**) Schematic diagram of low-temperature application of $Na_3V_{1.5}Al_{0.5}(PO_4)_3$ cathode, (**b**) Calculated DOS of $Na_3V_{1.5}Al_{0.5}(PO_4)_3$ and NVP, (**c**) CV profiles at sweep rate of $Na_3V_{1.5}Al_{0.5}(PO_4)_3$ of 0.2 mV s^{-1}. Reproduced with permission from ref. [80]. Copyright 2022, Elsevier. (**d**) SEM image of NVTP-0.5, (**e**) In-situ XRD patterns of the NVTP-0.5 cathode, (**f**) Rate performance of HC//NVTP-0.5 full cell. Reproduced with permission from ref. [81]. Copyright 2024, ACS. (**g**) Ex-situ XPS spectra of V 2p of NVP-Ga0.75, (**h**) GITT curves and D_{Na} of NVP-Ga0.75, (**i**) Cycling performances of different samples. Reproduced with permission from ref. [82]. Copyright 2024, Elsevier.

3.2. Doping with Multiple Transition Metals

In order to enhance the competitiveness of NASICON cathodes in terms of cost and performance, a lot of exploration has been conducted on low V content components. Single-element doping often comes with insufficient capacity or structural instability when used, and the strategic migration of combining different elements can synthesize the advantages of individual elements, thereby improving structural integrity and cycling stability.

3.2.1. Doping of Binary Groups

To obtain a new NASICON type compound, the strategy of binary cations doping is achieved by incorporating two different cations into V site of NVP. The doping of bimetallic materials achieves multi-electron transfer through the introduction of additional redox pairs (such as Mn, Fe, Cr) by doping active elements, thereby breaking through the capacity limit of NVP and achieving higher energy density. On the other hand, simultaneously introducing strong bond energies (such as Ni-O, Zr-O) or stepwise redox potentials of the doping elements to suppress the Jahn-Teller distortion of Mn^{3+} and alleviate lattice strain enables ultra-long cycle life. Moreover, the doping of these two elements can also expand the Na^+ transport channels and reduce the migration energy barrier by changing the lattice size and local electronic environment, thereby improving the rate performance.

For example, Chen et al. [83] prepared Na-V-Mn-Ni composites based on NASICON-type structures by sol-gel method with Mn and Ni partially replacing the V^{3+} position in NVP (Figure 9a). It has shown that the Ni ion

is relatively electrochemically inert and its strong Ni-O bond enhances the lattice stability and effectively suppresses the Jahn-Teller distortion of Mn^{3+} (Figure 9b). In addition, the electrochemical capacity of the electrode can be improved by utilizing the multi-electron transfer of V^{3+}/V^{4+}, Mn^{2+}/Mn^{3+}, and Ni^{2+}/Ni^{3+} in the NASICON structure. The composite achieves a high initial capacity of 80.1 mAh g^{-1} at an ultra-high multiplicity of 20 C, and maintain a remarkable capacity of 50.9 mAh g^{-1} after 10,000 cycles. The reversible changes of certain diffraction peaks during charge/discharge can be clearly observed by in-situ XRD, which can illustrate its excellent electrochemical reversibility from the side (Figure 9c). In addition to replacing V sites with Mn and Ni, Mn and Zr can also replace V sites to result in excellent performance. For instance, Wang et al. [84] synthesized a novel Zr-doped and surface carbon-coated $Na_{3.95}MnV_{0.95}Zr_{0.05}(PO_4)_3$/C (NMVZP0.05/C). The Zr^{4+} ion has a large ionic radius and strong Zr-O bond energy (Figure 9d). After doping, it not only expands the ionic transmission channel, but more importantly, acts as a "pillar" to stabilize the structure and suppresses lattice strain with a volume change of less than 8.5%, thus achieving a capacity retention rate of 83.1% after 1000 cycles at a 30 C rate. In addition, the initial discharge capacities of NMVZP0.05/C at −30, 25, and 60 °C were 61.4, 97.7, and 84.1 mAh g^{-1}, respectively, with corresponding Coulombic efficiencies of 92.8%, 94.5%, and 78.9% (Figure 9e). This is due to the key role of Zr doping in improving the ability of the material for wide temperature applications. Moreover, Li et al. [85] prepared a novel multi-electron reactive low strain $Na_{3.5}Fe_{0.5}VCr_{0.5}(PO_4)_3$/C (NFVCP/C) anode material by using Fe and Cr to replace V sites. Thanks to the multi-electron redox chemistry of V, the low-stress reaction of Fe and the high-potential redox of Cr, the ternary NFVCP/C cathode produced a fascinating energy density of 509.4 Wh kg^{-1}. The best NFVCP/C sample with a carbon content of 14.29 wt.% significantly increases the electronic conductivity and shows a reversible capacity with 93.0% retention of the upper capacity after 100 cycles at 0.5 C (Figure 9f). Besides, throughout the charge/discharge process, the calculated D_{Na^+} of NFVCP/C is comparable to or even higher than other NASICON-type phosphate cathodes (Figure 9g). The total density of states (DOS) of NFVCP shows a discontinuous pattern near the Fermi energy level region, suggesting a semiconducting nature (Figure 9h).

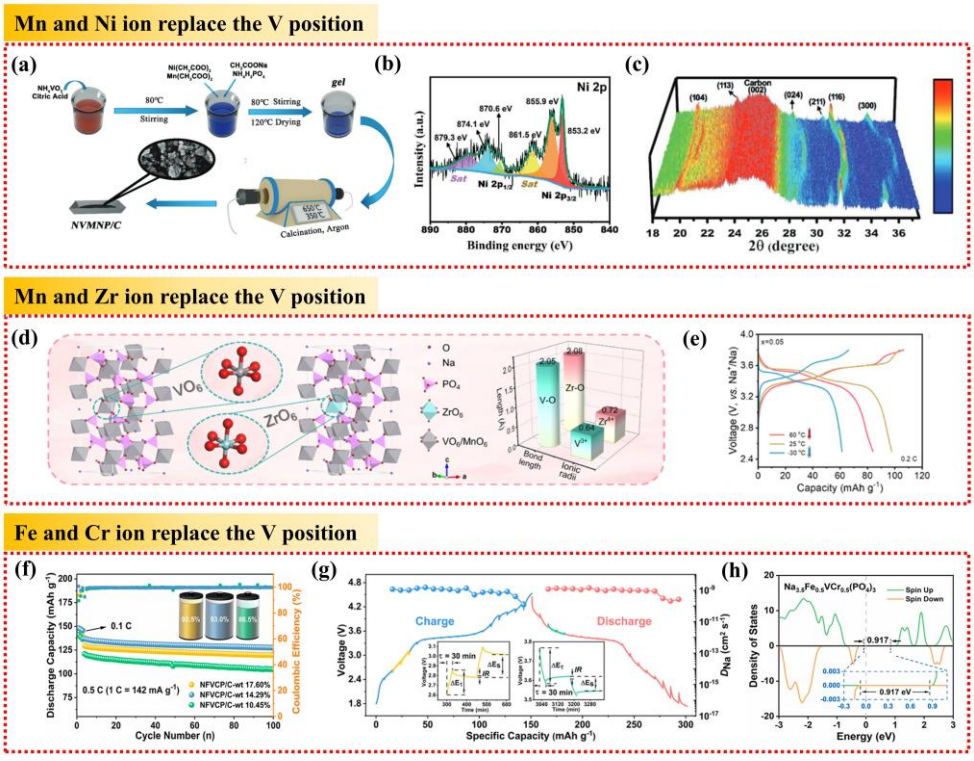

Figure 9. Examples of binary doping: (**a**) Schematic diagram of the preparation of NVMNP/C by sol-gel method. (**b**) The high-resolution XPS spectra of Ni 2p, (**c**) In-situ XRD patterns of NVMN-0.5 electrode. Reproduced with permission from ref. [83]. Copyright 2024, Wiley. (**d**) Schematic illustration of the crystal structure of NMVP and Zr-doped NMVP. (**e**) Initial charge/discharge curves of NMVZP/C-0.05. Reproduced with permission from ref. [84]. Copyright 2024, ACS. (**f**) Cycling performance of the samples with different carbon contents. (**g**) GITT curves along with representative magnified steps (insets) of NFVCP/C and corresponding D_{Na^+} values. (**h**) Total DOS of NFVCP. Reproduced with permission from ref. [85]. Copyright 2023, ACS.

However, due to the limited migration pathway of Na^+ ions, the highly ordered sodium rich structure leads to irreversible activation of high-pressure redox pairs. Therefore, it is necessary to study the further application of dual element NASICON type cathodes with extended ion channels and reversible reactions for SIBs.

3.2.2. Doping of Medium-Entropy

Due to the limited synergistic effects of binary metals systems, the regulation of configurational entropy by introducing more atoms has attracted growing interest, which can significantly expand the phase space of favorable atomic interactions. Hence, researchers have studied to investigate the doping of three to five different elements into NVP and proposed the concept of "medium-entropy", which are further based on binary doping research. The increase in configurational entropy can lead to more possible combinations of interactions, ultimately stabilizing the crystal structure and significantly improving the electrochemical performance of the electrode materials.

For example, Sun et al. [86] first prepared a new type of Fe/Mn/Co co-substituted NVP with nitrogen-doped carbon coating (NFMC) by a facile sol-gel method. The introduced heteroatom substitution activates more effective Na^+ to participate in electrochemical process and reinforce the structure. An extra high voltage platform at 3.8 V resulting from the multielement synergy ($Mn^{2+}/Mn^{3+}/Mn^{4+}$, Co^{2+}/Co^{3+}, V^{4+}/V^{5+}) is stably and reversibly existed in NFMC to supply added rate capacity (Figure 10a). It is noteworthy that the specific capacities of all doped samples exceed the theoretical specific capacity of NVP. Moreover, the final capacity of NFMC0.1 can still reach 133.2 $mAhg^{-1}$ after 100 cycles (Figure 10b). In addition, a secondary conductive framework was successfully developed through the integration of carbon and nitrogen species. Comprehensive experimental characterization combined with theoretical simulations confirmed the presence of Fe, Mn, and Co elements in both the bulk phase and the surface architecture (Figure 10c). Moreover, Wu et al. [87] utilized five metallic elements to partially substitute V atoms to prepare a medium-entropy cathode material ($Na_{3.2}V_{1.1}Ti_{0.2}Al_{0.2}Cr_{0.2}Mn_{0.2}Ni_{0.1}(PO_4)_3$, ME-NVP). On the side, ME-NVP undergoes single-phase processes at both plateaus of 3.4 and 4.0 V, which favors rapid diffusion of sodium and electrochemical reversibility because there is no phase separation caused by thermodynamic phase instability (Figure 10d). The symmetry change in the charge transfer resistance of ME-NVP indicates the important role of medium-entropy effects in enhancing mass and charge transfer, which is conductive to the sodium storage performance at the high-voltage plateau (Figure 10e). The weak chemical bonding between Na^+ ions and O atoms in the ME-NVP backbone channels facilitates the rapid diffusion of Na^+, which yields excellent rate properties. In addition, the cocktail effect of medium-entropy substitution of Al, Ti, Cr, Mn, and Ni elements can help the ME-NVP cathode to achieve the goals of long cycle life, high voltage plateau, high energy density, low attenuation, and low polarization simultaneously (Figure 10f).

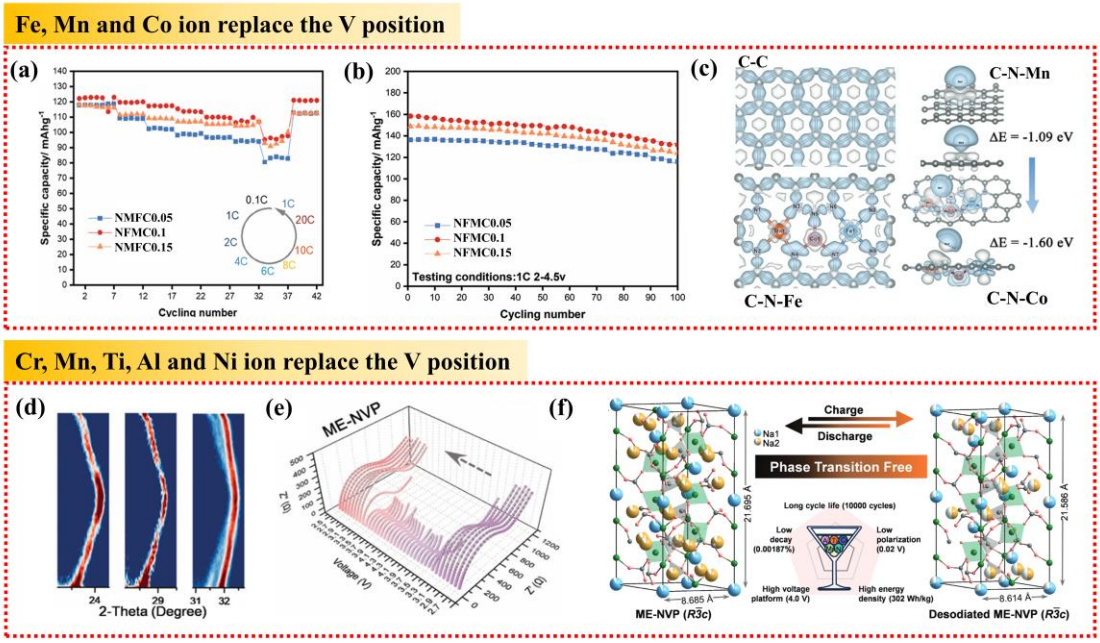

Figure 10. Examples of medium-entropy doping: (**a**) The rate performance of samples. (**b**) The cycling performance of the samples. (**c**) The simulated deformation charge densities. Reproduced with permission from ref. [86]. Copyright 2023, Wiley. (**d**) The contour plots of the in-situ XRD patterns of ME-NVP. (**e**) The in-situ EIS measurement of

ME-NVP cathode at the first charging/discharging cycle. (**f**) The schematic illustration for the sodium storage mechanism. Reproduced with permission from ref. [87]. Copyright 2025, Wiley.

By substituting multi-element doping to modulate the composition and achieve a medium-entropy state, which significantly increases the solid solubility of different transition metal (TM) species in one phase and promotes compatibility between TM species with different ionic radii. This compatibility helps to prevent large phase and lattice changes, thus maintaining the structural stability of the material. As a result, the medium-entropy material demonstrates stable operation at high voltages while maintaining high energy density and superior rate performance, thereby effectively stabilizing the main framework of the NASICON structure and addressing the long-standing reversibility issues associated with the activation of multiple redox pairs rate performance.

3.2.3. Doping of High-Entropy

Rather than relying on the function of a single dopant, high-entropy regulation exploits the cooperative interactions arising from multiple elemental species to tailor the thermodynamic and kinetic characteristics of electrode materials. The increased compositional complexity modifies the local atomic configuration and energy landscape, enabling simultaneous optimization of structural integrity and electrochemical activity. Such entropy-assisted regulation can facilitate ion migration, improve charge-transfer behavior, and stabilize the host framework against degradation induced by repeated electrochemical cycling. Furthermore, the presence of multiple redox-active centers broadens the accessible reaction chemistry and promotes more efficient utilization of lattice resources. Consequently, high-entropy materials have demonstrated considerable potential for achieving a balanced combination of high energy density, rapid charge-storage capability, and prolonged cycling stability.

For instance, Wang et al. [88] prepared a multicomponent entropy-regulated NASICON cathode $Na_3V_{1.5}(CrMnFeMgAl)_{0.5}(PO_4)_3$@C (HE-NVMP@C) by simultaneously introducing several heterovalent elements into the host lattice through a sol-gel synthesis route (Figure 11a). HE-NVMP@C exhibits outstanding tolerance to high current densities and maintained considerable reversible sodium-storage capability even under fast charge/discharge conditions, indicating substantially improved reaction kinetics (Figure 11b). Electrochemical impedance analysis revealed a lower interfacial resistance and more favorable ion/electron transport behavior compared with the undoped counterpart (Figure 11c). The enhanced electrochemical characteristics can be primarily attributed to the collective influence of the multielement configuration. The increased chemical complexity reshaped the local atomic environment and produced a more uniform energy landscape for sodium migration, facilitating rapid ionic diffusion throughout the framework. At the same time, the entropy-induced stabilization effect strengthened the resistance of the crystal lattice against structural distortion and degradation during repeated cycling. The coexistence of different cation species also promoted a more balanced redistribution of electronic states, which contributed to improved charge-transfer processes and reduced polarization. In contrast to the first study, which primarily focused on entropy-induced structural stabilization, Zhang et al. [89] highlighted the role of high-entropy regulation in optimizing electronic structure and Na^+ transport kinetics. A homogeneous high-entropy NASICON framework was constructed by introducing multiple cations (V, Fe, Mg, Cr, and Zr) into the host lattice, with elemental mapping confirming their uniform distribution throughout the material (Figure 11d). The optimized cathode exhibited excellent rate capability, retaining 99.9 mAh g^{-1} at 20 C, while the capacity contribution above 3.0 V increased by nearly 10%, indicating enhanced utilization of high-voltage Mn redox reactions (Figure 11e). Density-of-states calculations revealed a narrowed bandgap and the elimination of trap states near the Fermi level, which promoted electron transport. Meanwhile, theoretical simulations demonstrated reduced Na^+ diffusion barriers and wider migration pathways (Figure 11f). The combined enhancement of electronic conductivity, ionic transport, and structural stability resulted in lower polarization, reduced impedance, and superior electrochemical performance. Distinct from the second study, which primarily focused on electronic-structure modulation and charge-transport enhancement, Liao et al. [90] emphasized the synergistic coupling between high-entropy regulation and multielectron redox chemistry. A high-entropy NASICON cathode $Na_3V_{1.47}(Fe, Al, Ga, Mg, Mn)_{0.5}Mo_{0.01}Nb_{0.02}(PO_4)_3$ (HE-NVP-MN) was constructed by incorporating multiple cations into the NVP framework, forming a compositionally complex crystal structure with uniformly distributed active and inactive metal species (Figure 11g). Cyclic voltammetry revealed highly reversible redox behavior during the initial cycles, while DFT calculations demonstrated substantially reduced Na^+ migration barriers compared with the undoped counterpart, indicating accelerated ion diffusion kinetics (Figure 11h). The corresponding energy profiles further confirmed a more favorable migration pathway for sodium transport (Figure 11i). Moreover, high-entropy substitution slightly narrowed the bandgap and promoted charge transfer, resulting in lower polarization and enhanced reaction kinetics. Combined with the activation of reversible $V^{3+}/V^{4+}/V^{5+}$ and $Mn^{2+}/Mn^{3+}/Mn^{4+}$ redox

couples, the entropy-driven design enabled improved rate capability, exceptional cycling durability, and high energy density.

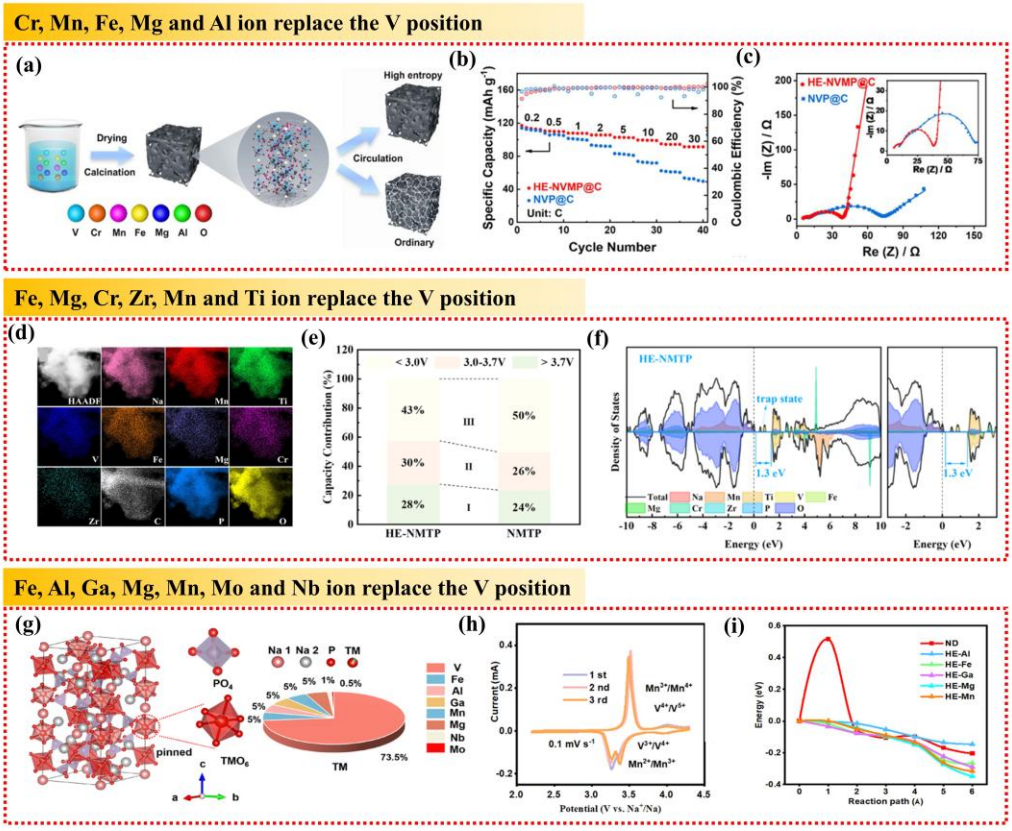

Figure 11. Examples of high-entropy doping: (**a**) Schematic of the synthesis and the circulation morphology of HE-NVMP@C. (**b**) Rate performance. (**c**) EIS spectra of the two materials after 5000 cycles at 20 C. Reproduced with permission from ref. [88]. Copyright 2024, RSC. (**d**) HAADF-STEM image and the corresponding elemental mappings for HE-NMTP material. (**e**) Capacity contribution of NMTP and HE-NMTP cathodes in different voltage ranges at 0.1 C. (**f**) The DOS of HE-NMTP. Reproduced with permission from ref. [89]. Copyright 2024, Elsevier. (**g**) Schematic crystal structure of HE-NVP-MN. (**h**) CV curves of HE-NVP-MN in the first three cycles at 0.1 mV s^{-1}. (**i**) The corresponding migration energy profiles and diffusion barriers in ND and HE. Reproduced with permission from ref. [90]. Copyright 2025, Elsevier.

In short, the synergistic effect of multiple elements increases the configurational entropy and induces moderate lattice distortion, which stabilizes the crystal structure and suppresses irreversible structural degradation during cycling. Meanwhile, the modified local coordination environment and enlarged ion diffusion channels facilitate faster Na^+ transport and improve electronic conductivity. In addition, high-entropy doping can regulate the electronic structure, activate additional redox couples, and promote reversible multi-electron transfer reactions, thereby increasing the operating voltage and energy density. The homogeneous distribution of diverse elements also helps inhibit transition-metal migration, reduce polarization and voltage hysteresis, and enhance the reversibility of electrochemical reactions. As a result, high-entropy cathodes generally exhibit improved capacity, rate capability, cycling stability, and energy density compared with their conventional counterparts.

4. Vanadium-Free Positive Electrode

In order to minimize the use of V, many research groups are now studying V-free cathode, i.e., replacing all the V sites in NVP with transition metals, so as to achieve excellent electrochemical performance while reducing the amount of hazardous substances V [91]. The central strategy involves activating multi-electron redox chemistry through the synergistic combination of earth-abundant transition metals (Fe, Mn, Cr, Ti, Zr), which not only boosts reversible specific capacity and energy density but also introduces additional redox centers that contribute to overall capacity.

For example, using the Fe to completely replace V position, Lu et al. [92] prepared $NaFePO_4$/C by the combination of low-temperature sintering and ball milling. Figure 12a shows the structure of M-$NaFePO_4$, which

delivers a reversible capacity of 134 mAh g^{-1} and still demonstrates decent capacity-retention of 75.4% over 1000 cycles. Notably, the fabricated $NaFePO_4$/C//HC full cell has an energy density of up to 169.9 Wh kg^{-1} and has reversible capacities of 112.8, 106.4, 98.9, and 88.1 $mAhg^{-1}$ at rates of 0.5, 1, 2, and 5 C, respectively (Figure 12b). In the s-XAS spectrum of a typical Fe-L3 edge, the intensity of the absorption peak located at 710 eV increases after charging to 3.8 V, indicating a transition from Fe^{2+} to Fe^{3+}. After charging to 4.6 V, the main component of Fe is Fe^{3+}. When discharged to 1.5 V, the absorption spectra returned to the initial state, indicating that the oxidation process is highly reversible (Figure 12c). In addition to completely replacing V with a single element, there is also the possibility with a bimetallic element. For instance, Ren et al. [93] successfully fabricated free-standing $Na_3MnTi(PO_4)_3$/C (NMTP/C) nanofibers via electrospinning followed by high-temperature pyrolysis. Rietveld-refined XRD patterns (Figure 12d) demonstrate that the material possesses a rhombohedral R-3C NASICON crystal structure with spacious three-dimensional Na^+ diffusion channels. The synergistic redox couples of $Mn^{2+}/Mn^{3+}/Mn^{4+}$ and Ti^{3+}/Ti^{4+} endow the material with multi-electron reaction capability, as reflected by three distinct charge-discharge voltage platforms at 2.16 V, 3.45 V and 4.04 V in the initial GCD curves (Figure 12e). Benefiting from the cross-linked carbon nanofiber network, the NMTP/C electrode delivers excellent high-rate cycling durability, retaining approximately 92% of its initial capacity after 500 cycles at 5 C (Figure 12f). In addition to single and binary metal doping modification, this self-supporting multi-metal composite fiber strategy exhibits outstanding comprehensive sodium storage performance. Besides, Rao et al. [94] successfully synthesized NASICON-type cathode materials of $Na_3MnTi_{0.5}Zr_{0.5}(PO_4)_3$ by using Mn, Ti and Zr completely replacing V sites. The ionic radius of Ti^{4+} (0.605 Å) is smaller than that of Zr^{4+} (0.72 Å). This size difference allows Ti^{4+} to effectively displace Zr^{4+}, leading to the precise formation of NASICON structures at any Ti/Zr ratio. The crystal structure of NMZP consists of MnO_6 and ZrO_6 octahedral units that connected coaxially by PO_4 tetrahedra, forming a three-dimensional channel, which provides a wide space for the migration of Na^+ (Figure 12g). The substitution of Ti not only enlarges the diffusion channel of Na^+, but also shortens the Mn-O bond length, resulting in a more stable structure. In addition, the ingenious presence of Ti^{3+}/Ti^{4+} acts as a strong barrier and effectively suppresses the Jahn-Teller effect of Mn^{3+}, thus tremendously stabilizing the overall structure of the material (Figure 12h). Ti substitution not only significantly enhances the interfacial stability of the material, but also effectively reduces the charge transfer resistance. It is important to emphasize that there is no significant change in the R_{ct} value during pre-charging and post-discharging, further demonstrates the stability of the material structure (Figure 12i).

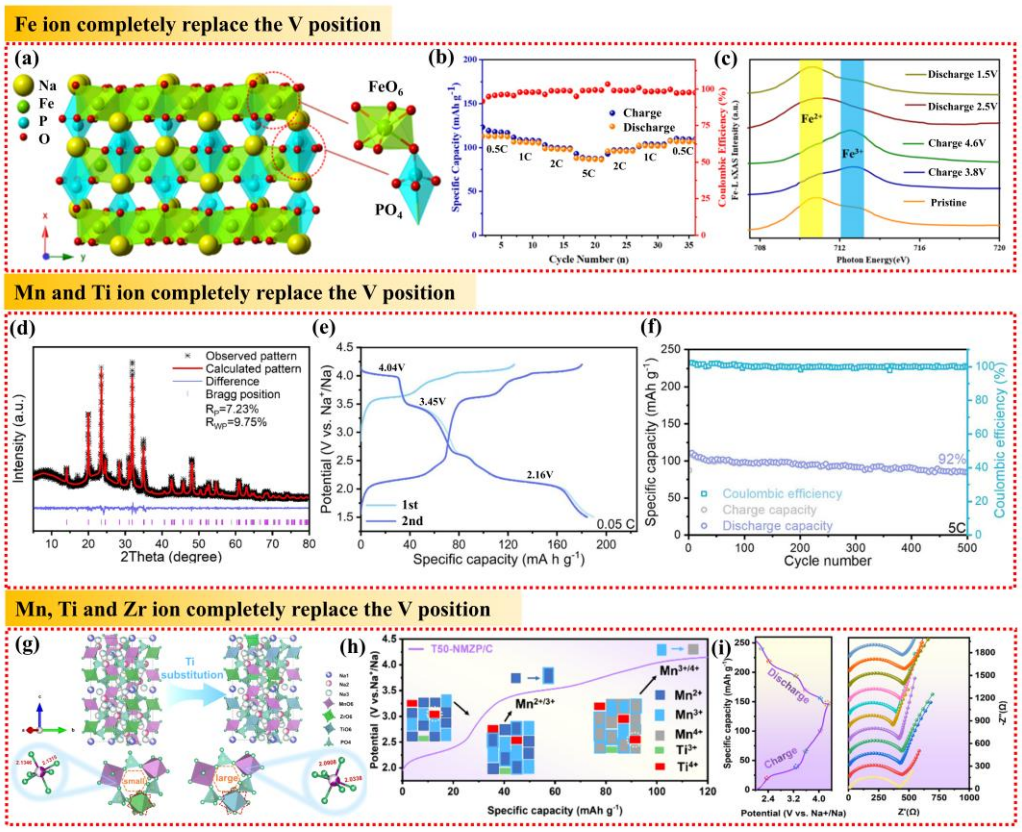

Figure 12. Examples of vanadium-free doping: (**a**) Illustrations of the structure of M-$NaFePO_4$. (**b**) Rate capability. (**c**) Fe L-edge s-XAS at different charge states. Reproduced with permission from ref. [92]. Copyright 2023, AIP. (**d**) Rietveld

structural refinement of XRD patterns. (**e**)The GCD curves of NMTP/C nanofibers electrodes. (**f**) The cycling stability of NMTP/C at 5 C. Reproduced with permission from ref. [93]. Copyright 2024, Elsevier. (**g**) Schematic of the crystal structure. (**h**) Schematic diagram of the material structure change during charging and discharging. (**i**) Ex-situ impedance plots of T50-NMZP/C at different voltages. Reproduced with permission from ref. [94]. Copyright 2025, Elsevier.

NVP has attracted much attention due to its high theoretical capacity and splendid cycling stability, but the potential toxicity and cost of vanadium limit its practical application. As a result, by moving beyond vanadium and leveraging cost-effective, abundant elements with careful structural and morphological optimization, vanadium-free phosphate cathodes can deliver a compelling combination of high energy density, exceptional cycle life, and high-rate performance, thereby offering a sustainable and economically viable pathway for next-generation sodium-ion batteries.

5. Anionic Site Doping

Anion doping is an effective strategy to enhance the performance of NVP, a cathode material for SIBs [95–98]. By introducing anions such as Si^{2-}, S^{2-}, MO_4^- or F^- to partially replace the PO_4^{3-} groups, the structural stability, electronic conductivity, and Na^+ diffusion kinetics can be significantly enhanced. Specifically, anion doping can introduce impurity energy levels into the energy band structure of the material, narrowing the band gap and enhancing the electrical conductivity. In addition, anion doping can inhibit lattice distortion during charging/discharging, which reduces structural degradation, thus substantially improving cycling stability.

For instance, Chen et al. [99] prepared $Na_{3.1}V_2(PO_4)_{2.9}(SiO_4)_{0.1}$/C@rGO using a freeze-drying assisted sol-gel method to introduce Si and combine it with conductive reduced graphene oxide (rGO) to improve the electrical conductivity and electrochemical properties (Figure 13a). The kinetic properties of the Si0.1-NVP/C@rGO are intensively investigated through the GITT method. The minimum value of D_{Na+} occurs around 3.4 V, which is attributed to the strong interactions between Na^+ and the host skeleton during the phase transition reaction (Figure 13b). Figure 13c reveals the rate performance of all samples tested at diverse rates from 0.1 to 6 C. Si0.1-NVP/C@rGO composite displays a discharge capacity of 113.6, 107.3, 104.9, 104.1, 100.2 and 96 mAh g^{-1} at current densities of 0.1, 0.5, 1, 2, 4 and 6 C, respectively. When the current density is restored from 6 C to 0.1 C, the capacity could be restored to 111.8 mAh g^{-1}, indicating excellent multiplicative performance (Figure 13c). In addition, EIS tests confirm that the D_{Na+} of Si0.1-NVP/C@rGO is much higher than that of NVP/C (Figure 13d). This is because the large ionic radius of Si^{4+}, Si substitution can expand the channels for Na^+ migration and effectively promote ionic conductivity. Meanwhile, Si doping facilitates the formation of a porous structure and improves the interconnection between the active substance and the electrolyte. In addition, the introduction of rGO can inhibit the agglomeration of the active particles and construct a carbon network, which significantly improves the electrical conductivity. Nevertheless, their performance enhancement is still significantly reliant on the introduction of external carbon materials. Based on this, researchers shifted their focus to explore intrinsic modification strategies that do not rely on carbon encapsulation. For example, Liu et al. [100] innovatively replaced PO_4^{3-} with MoO_4^{2-} (Figure 13e). The XPS spectra of Mo 3d shows the presence of Mo^{5+} and Mo^{6+} in the form of mixed valence of the element Mo (Figure 13f). In addition, first-principle calculations confirm that this doping could effectively reduce the band gap of the material and significantly enhance the intrinsic conductivity (Figure 13g). This anionic doping strategy not only avoids the complex carbon capping process, but also realizes an excellent capacity of 84.2 mAh g^{-1} at an ultra-high multiplicity of 50 C, which opens up a new avenue for the development of high-performance NVP materials. Although cationic and anionic doping strategies have significantly enhanced the electrochemical properties of NVP materials, their practical applications are still limited by low vibrational densities and complex synthesis processes. Recently, Song et al. [101] proposed a groundbreaking high-temperature shock (HTS) strategy to synthesize large-sized, high-density $Na_3V_2(PO_4)_2F_3$ particles, which achieves high electronic conductivity and suppresses interfacial side reactions (Figure 13h). The HTS-NVPF exhibits a tap density of 1.51 g cm^{-3}, exceeding that of $LiFePO_4$, which is beneficial for achieving a higher volumetric energy density in the resulting batteries (Figure 13i). Due to its tight structure, the HTS-NVPF electrode exhibits a significant capacity retention of 94.2% after 200 cycles (Figure 13j). This is because that the introduction of F^- not only stabilizes the crystal framework but also effectively suppresses the formation of NVP impurities caused by F loss, ensuring high structural integrity and cycling stability.

Anionic doping at the PO_4^{3-} sites has emerged as a versatile and effective approach to enhance the electrochemical performance of polyanionic cathode materials for sodium-ion batteries. Despite the differences in dopant species, a common feature lies in the modulation of the local crystal and electronic structures, the substitution of tetrahedral anions expands the lattice parameters and enlarges the migration channels for Na^+, thereby facilitating ionic diffusion kinetics. Concurrently, the altered electronic environment effectively narrows

the band gap and enhances the intrinsic electronic conductivity, as consistently evidenced by reduced charge-transfer resistance and improved rate capability. Furthermore, anionic substitution contributes to stabilizing the crystal framework and suppressing the formation of undesirable impurities during synthesis, ensuring superior structural integrity and long-term cycling stability. These shared advantages highlight the broad applicability of anion engineering in overcoming the key limitations of phosphate-based cathodes for high-performance SIBs.

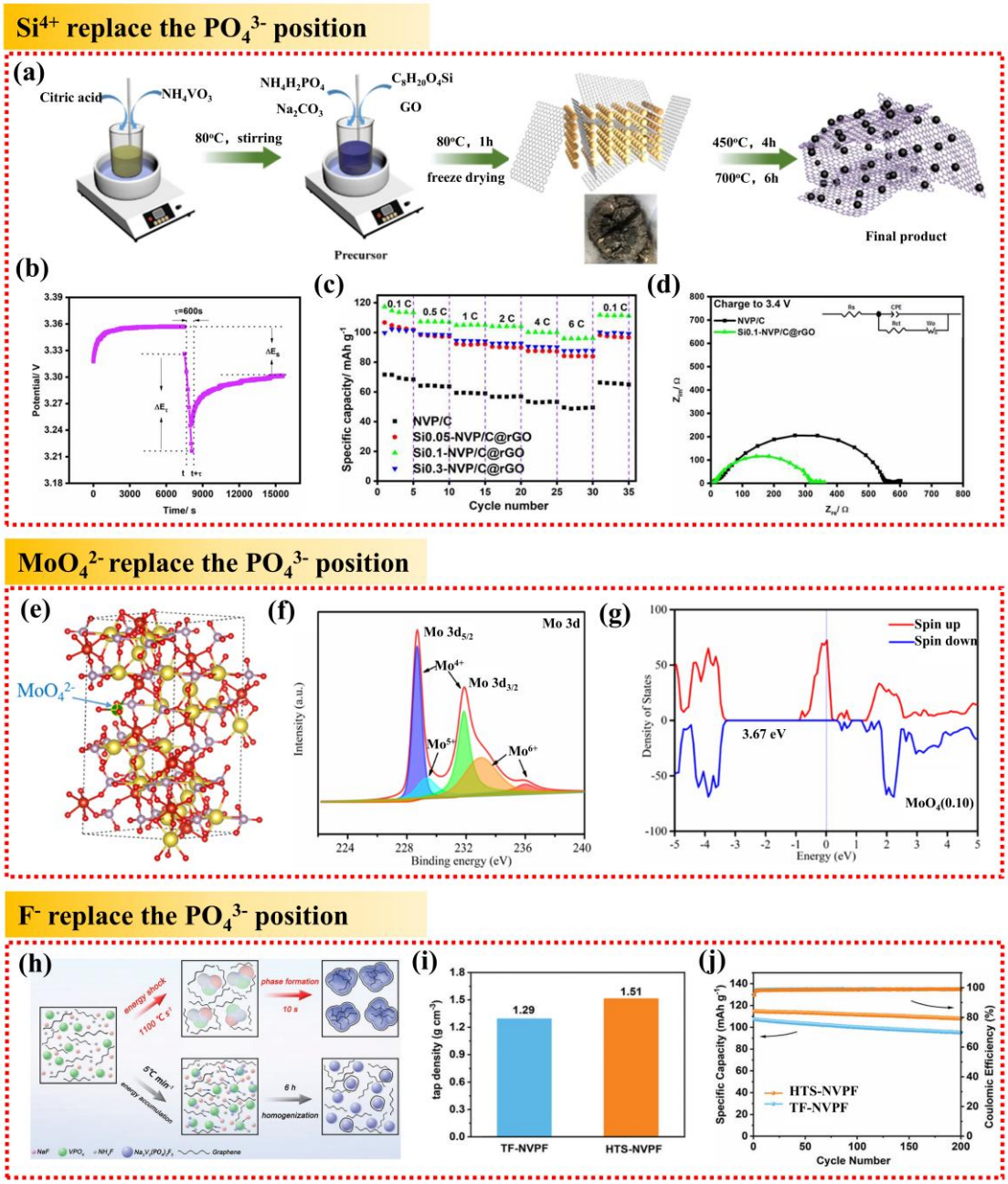

Figure 13. Examples of anionic site doping: (**a**) Synthesis process of Si0.1-NVP/C@rGO using freeze-drying assisted sol-gel method. (**b**) GITT curves. (**c**) Rate performance of all samples. (**d**) Nyquist plots of the samples. Reproduced with permission from ref. [99]. Copyright 2020, Elsevier. (**e**) Structural diagram of NVP-MoO_4. (**f**) XPS of Mo 3d. (**g**) Density of states of NVP-MoO_4. Reproduced with permission from ref. [100]. Copyright 2022, Elsevier. (**h**) Schematic illustration of formation mechanism of the NVPF formed by HTS and TF. (**i**) Tap density of the HTS-NVPF and TF-NVPF. (**j**) Long cycle stability at 1 C rate. Reproduced with permission from ref. [101]. Copyright 2024, Wiley.

6. Multi-Site Doping

As can be seen from the previous content, the single-site doping (e.g., Na-site, V-site, or PO_4-site) has made significant progress. However, single-site doping is often difficult to optimize the electronic conductivity, structural stability and ion diffusion kinetics of the material simultaneously. The multi-site doping strategy is able

to optimize the material properties more comprehensively by synergistically modulating multiple sites of the material (e.g., co-doping of Na site with V site, Na site with PO_4^- site, V site with PO_4^- site, or even three sites). This strategy not only introduces multiple defects and active sites, but also further broadens the Na^+ transport channel and lowers the diffusion energy barrier through the synergistic effect of different sites [102,103], which significantly enhances the electrochemical properties of the materials. In this chapter, we will systematically summarize the application of multi-site doping in NVP materials [55,104], explore the effects of different doping modes on the structure, electronic conduction and electrochemical behavior of the materials, and analyze their potential applications in SIBs. The in-depth study of multi-site doping is expected to provide new ideas for the development of high-performance NVP materials and promote the commercialization of SIBs technology.

6.1. Na Site and V Site Co-Doping

Unlike conventional single-site modification, the simultaneous regulation of alkali-metal and transition-metal sublattices provides a more comprehensive strategy for optimizing NASICON cathodes. By introducing larger cations at Na sites and heteroatoms at transition-metal sites, the local coordination environment, lattice geometry, and electronic structure can be synergistically tailored. The Na-site substitution enlarges diffusion channels and facilitates sodium-ion migration, whereas transition-metal-site substitution stabilizes the framework, suppresses structural distortion, and modulates redox behavior. Such cooperative regulation effectively lowers Na^+ diffusion barriers, improves charge-transfer kinetics, and enhances structural durability during repeated cycling. In addition, the altered electronic environment promotes more reversible redox reactions and reduces polarization. As a result, dual-site engineering enables simultaneous improvements in rate capability, cycling stability, and energy-storage efficiency, demonstrating a promising route for the rational design of high-performance NASICON-type sodium-ion battery cathodes.

Doping of Na sites is mainly achieved by introducing alkali metal ions with larger radii (e.g., K^+). Doping of V sites is usually achieved by partially replacing the V element to reduce the toxicity and cost of the material, while introducing additional redox pairs. For example, Zhou et al. [105] prepared a series of $Na_{4-x}K_xFeV(PO_4)_3$@C composites by sol-gel method and partially replaced V with Fe, an environmentally friendly and cost-effective transition element, and doped K at the Na site (Figure 14a). The lower potential difference for the $Na_{3.9}K_{0.1}FeV(PO_4)_3$@C explains that the K-doped sample has a lower polarization and faster Na^+ diffusion kinetics, which are conductive to the reversible insertion/extraction of Na^+ (Figure 14b). The K-doped electrodes exhibit lower charge transfer resistance compared to the pristine samples. K-doped NFVP not only promotes the transport of Na^+, but also improves the electronic conductivity of the material, thus enhancing the electrochemical properties (Figure 14c). In addition, for $Na_4VMn(PO_4)_3$, which has three-dimensional structure and high operating voltage, and also possesses great potential as a cathode material for SIBs. However, the Jahn-Teller effect originating from the formation of Mn^{3+} during sodium (de)intercalation and the slow diffusion mechanism of Na^+ hinder its performance, leading to capacity decay and structural instability. Chen et al. [106] achieved $Na_{3.3}K_{0.1}Ca_{0.1}VMn_{0.8}Zr_{0.2}(PO_4)_3$ (NKCMVP-Zr0.2) synergistically modulating the coordination environment and realizing a one-step denaturation reaction of NMVP by introducing Zr^{4+} and K^+/Ca^{2+} to the Mn and Na sites, respectively (Figure 14d). The GITT curves of NKCMVP-Zr0.2 exhibit a voltage plateau during both charging and discharging. Moreover, the D_{Na^+} values during charging/discharging maintain a stable value of Na^+ diffusion coefficient of 1.01×10^{-10} cm^2 s^{-1}, which could be attributed to the widening of Na^+ diffusion channels by Zr^{4+} doping (Figure 14e). In addition, the XRD pattern of NKCMVP-Zr0.2 exhibits only a slight peak displacement at 3.8 V without the presence of new peaks, suggesting that a single-phase reaction mechanism is realized during the whole sodium removal process. When the discharge reaches 2.5 V, the diffraction peaks of both NKCMVP and NKCMVP-Zr0.2 electrodes almost return to their original positions, explaining that the Na^+ insertion/extraction process is well reversible (Figure 14f). The DOS plots show the absence of band gap in the spin up portion, indicating metallic nature. This demonstrates that the substitution of Zr^{4+} enhances the metallic abundance of the material, which may be attributed to the introduction of the 4d Zr element increasing the number of electrons in the material system and hence the electronic conductivity (Figure 14g).

In a word, the advantages of Na-site and V-site co-doping lies in its ability to comprehensively modulate the ionic and electronic conduction properties of the materials, while further enhancing the structural stability and electrochemical properties through multi-element synergistic effects. However, optimization of co-doping requires consideration of elemental coexistence and precisely control the doping concentrations to prevent the formation of impurity phases or causing lattice distortion. Future research can further explore multi-element co-doping systems systematically. By integrating theoretical calculations with advanced characterization techniques,

researchers can clarify the mechanism of the rule of co-doping in performance regulation, thereby promoting the development of high-performance SIBs cathodes.

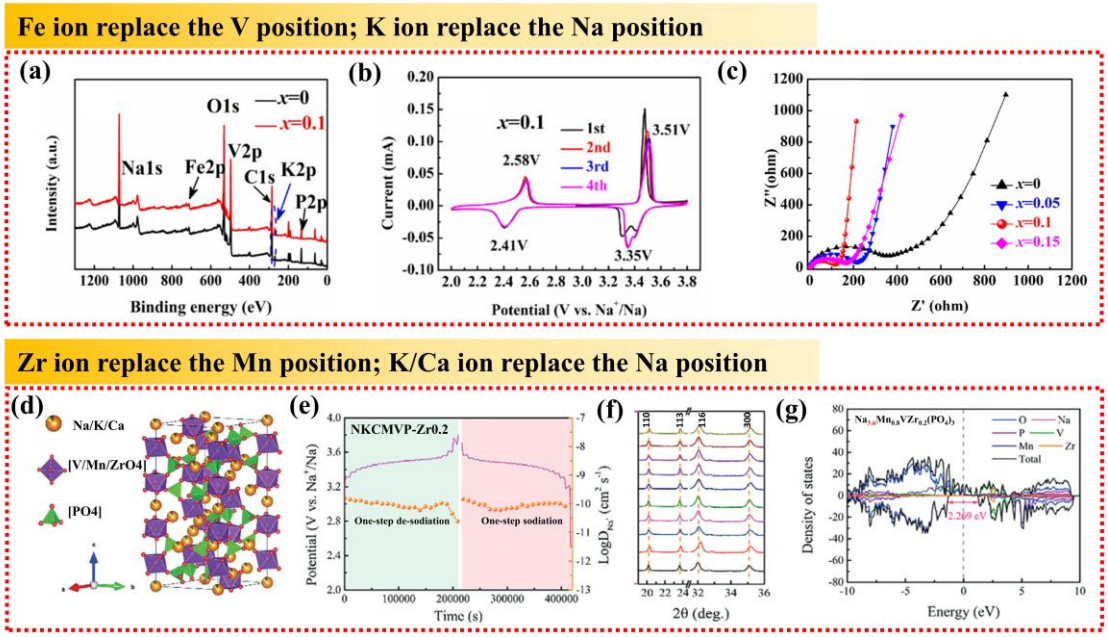

Figure 14. Examples of Na site and V site co-doping: (**a**) Full XPS survey spectra of $Na_4FeV(PO_4)_3$@C and $Na_{3.9}K_{0.1}FeV(PO_4)_3$@C. (**b**) CV curves of $Na_{3.9}K_{0.1}FeV(PO_4)_3$@C. (**c**) EIS spectra of samples. Reproduced with permission from ref. [105]. Copyright 2025, Elsevier. (**d**) Schematic crystal structure of NKCMVP-Zr0.2. (**e**) GITT curves and diffusion coefficient of sodium ions of NKCMVP-Zr0.2. (**f**) Ex-situ XRD patterns NKCMVP-Zr0.2 electrodes. (**g**) DOS of $Na_{3.6}VMn_{0.8}Zr_{0.2}(PO_4)_3$. Reproduced with permission from ref. [106]. Copyright 2025, Wiley.

6.2. Na Site and PO_4^{3-} Site Co-Doping

Na-site and PO_4^{3-} site co-doping strategies are used to further optimize the comprehensive properties of NVP materials by synergistically modulating the Na^+ storage sites and PO_4^{3-} anionic backbone. Na-site doping (e.g., Li^+, K^+, etc.) can modulate the lattice parameters, broaden the Na^+ migration channels, and improve the ionic conductivity, while PO_4-site doping (e.g., SiO_4^{4-}, F^-, etc.) can enhance the electronic conductivity of the material and inhibit the structural distortion during charging/discharging by changing the electronic structure and bonding properties of the anionic backbone. By rationally designing the co-doping of Na and PO_4 sites, it can not only stabilize the crystal framework and reduce the volume change, but also synergistically optimize the Na^+ transport path and charge transfer efficiency, which can significantly enhance the rate performance and cycling stability of NVP materials.

For example, Wu et al. [107] developed dual-site substitution strategy by simultaneously introducing K^+ into the Na sublattice and F^- into the polyanionic framework ($N_{0.92}K_{0.08}VPF$/C) through a sol-gel-assisted synthesis route, enabling concurrent regulation of crystal structure and electrochemical kinetics (Figure 15a). The CV curves of $N_{0.92}K_{0.08}VPF$/C indicate that K^+ doping effectively reduces electrochemical polarization and suppresses voltage hysteresis in charging/discharging in high-performance SIBs, which imply that minimal polarization and highly reversible phase transitions take place during sodiation/desodiation (Figure 15b). At 0.2 C, $N_{0.92}K_{0.08}VPF$/C shows higher capacity and cycling stability than the other three samples, as well as a high Coulombic efficiency of 92% after 100 cycles (Figure 15c). After K^+ doping, the cell parameters a, b, and c become larger, indicating that K^+ doping broadens the Na^+ migration channel effectively, thereby facilitating faster Na^+ transport (Figure 15d). Meanwhile, the stronger electronegativity of F^- modified the local electronic environment, strengthened the framework stability, and promoted charge-transfer kinetics. In addition, Dou et al. [108] proposed a cation-anion simultaneous conditioning strategy to prepare $Na_{3.24}K_{0.10}V_{2.01}(PO_4)_{2.94}(SiO_4)_{0.14}$ (KSi-NVP) cathode materials. In this case, the K^+ is introduced into the column ionic sites to enhance the structural stability of the NVP crystals, which significantly improving the cycle life of the cathode material. Meanwhile, the replacement of PO_4^{3-} of the same structure with the anion SiO_4^{4-} introduces an additional Na^+ component and improves the Na^+ storage capacity (Figure 15e). The KSi-NVP cathode provides a high capacity of 116.3 mAh g^{-1} at 0.5 C, very close to the theoretical capacity (117 mAh g^{-1}) (Figure 15f). The co-doped material exhibited enlarged lattice parameters,

improved Na^+ diffusion kinetics, lower charge-transfer resistance, and superior rate capability. More importantly, the synergistic effect of K and Si significantly mitigated structural degradation, maintaining nearly unchanged cell volume and crystal integrity after prolonged cycling (Figure 15g).

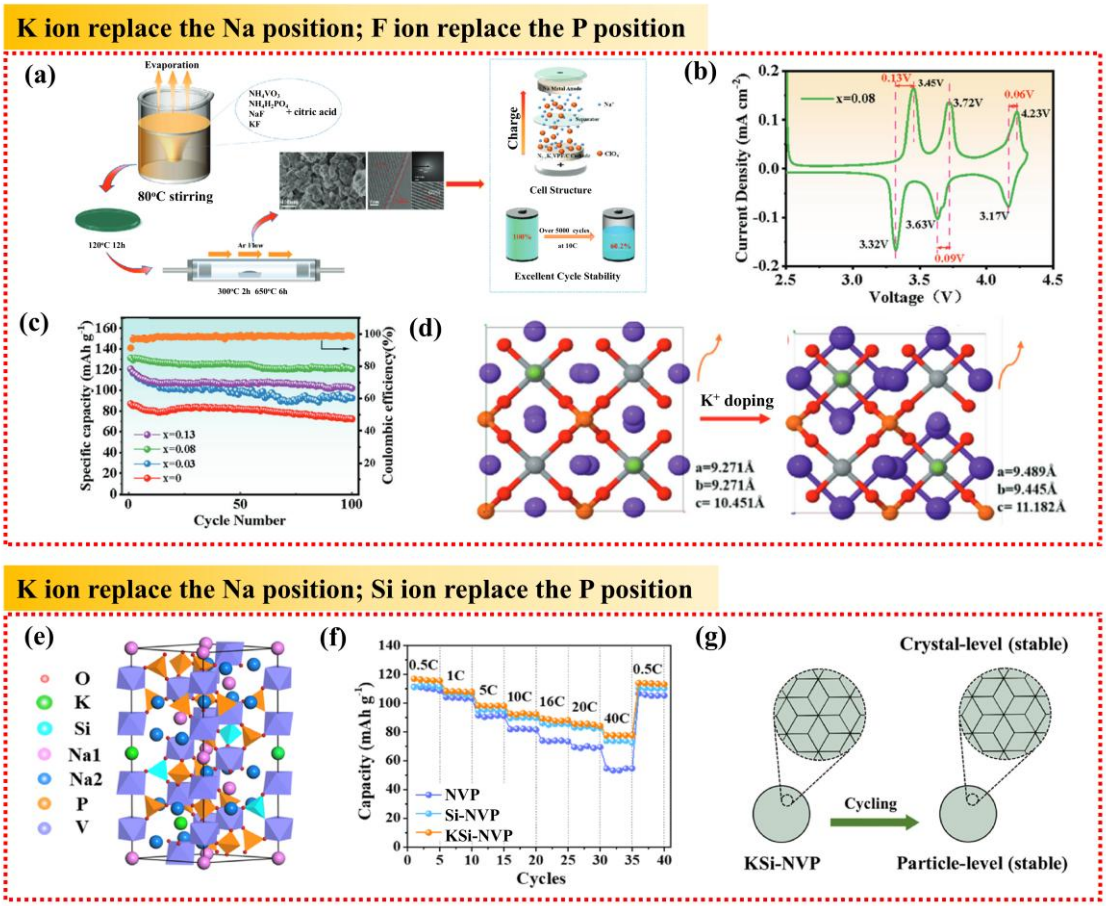

Figure 15. Example of Na site and PO_4^{3-} site co-doping: (**a**) Schematic illustrations for the synthesis process of $N_{1-x}K_xVPF/C$. (**b**) Cyclic voltammetry curves of $N_{1.92}K_{0.08}VPF/C$. (**c**) Cycling performance of $N_{1-x}K_xVPF/C$. (**d**) NVPF crystal changes before and after K doping. Reproduced with permission from ref. [107]. Copyright 2024, Wiley. (**e**) Schematic illustration of the crystal structure of the as-designed KSi-NVP. (**f**) Rate performance of samples. (**g**) Schematic illustration of the cycling processes of KSi-NVP cathode particles. Reproduced with permission from ref. [108]. Copyright 2023, Elsevier.

In summary, the Na-site and PO_4-site co-doping strategy significantly enhances the electrochemical properties of NVP materials by simultaneously modulating the Na^+ transport channel and anionic skeleton structure. Na-site doping (e.g., Li^+, K^+, etc.) can optimize the lattice parameters, broaden the Na^+ diffusion path, and increase the ionic conductivity, while PO_4^{3-} site doping (e.g., SiO_4^{4-}, F^-, MoO_4^{2-}, etc.) enhances the electronic conductivity of the material and suppresses the structural distortion during charging and discharging by changing the anionic coordination environment and electronic structure. The synergistic effect of the two not only stabilizes the crystal framework, but also reduces the Na^+ migration energy barrier, which significantly improves the rate performance and cycling stability of the materials.

6.3. V Site and PO_4^{3-} Site Co-Doping

The co-doping strategy of V-site and PO_4-site enhances the electrochemical performance of NASICON-type cathode materials by synergistically modulating the redox centers of the transition metals and the framework structure of polyanions. The introduction of doping ions such as Al^{3+}, Cr^{3+}, and Ti^{4+} at the V-site can effectively regulate the electronic structure of the transition metals, enhance the redox activity and inhibit the side reactions. Meanwhile, at the PO_4^{3-} site, SiO_4^{4-}, BO_3^{3-} and other anionic group substitutions at the PO_4 site can optimize the crystal coordination environment and improve the structural stability and Na^+ transport kinetics. Besides, this two-

site synergistic doping strategy eliminates the low-voltage plateau, thereby improving the average operating voltage and energy density.

For instance, using solid-phase sintering, Wang et al. [109] realized a dual-anion/cation regulation strategy through a facile solid-state synthesis by substituting Al^{3+} for V sites in the NVPF framework (Figure 16a). Al incorporation effectively modified the local electronic environment of V, enhanced fluorine retention during calcination, and significantly suppressed the formation of the electrochemically unfavorable NVP impurity phase. The optimized $Na_3V_{1.9}Al_{0.1}(PO_4)_2F_3$ delivered excellent rate capability, maintaining 103 mAh g^{-1} at 10 C and exhibiting nearly full capacity recovery upon returning to low current densities (Figure 16b). The in-situ XRD further revealed highly reversible phase evolution during Na^+ insertion/extraction, with the tetragonal NVPF framework remaining intact after cycling (Figure 16c). Moreover, the stabilization of F preserved the high-voltage characteristics of NVPF, while Al substitution reduced the bandgap and accelerated charge-transfer kinetics. Consequently, the synergistic effects of fluorine retention, enhanced electronic conductivity, and improved structural reversibility resulted in superior rate performance and long-term cycling stability. In addition, Li et al. [110] instead added Cr and Si to NVP to form $Na_3V_{1.9}Cr_{0.1}(PO_4)_{2.9}(SiO_4)_{0.1}$ (NVP-CS) by a simple solid-phase method (Figure 16d). As a result, the NVP-CS boasts an initial capacity of 102.2 mA h g^{-1} and a capacity retention rate of over 90% at 1 C (Figure 16e). The introduction of inert Cr can act as a reliable support in the crystals, thus improving the stability of the electrodes. On the other hand, the introduction of low molecular weight Si improves the theoretical capacity of the material. A significantly reduced band gap and the emergence of two independent impurity energy levels for V and O are observed in NVP-CS (Figure 16f). Additional electrons introduced by Cr and the extra V and O electron energy levels contributed by Si are coexisting in NVP-CS. Superior electrochemical properties of NVP-CS can be expected by the enhanced conductivity and the promoted redox reaction ability of V. In addition to single-element doping, high-entropy doping is also a well-established method. For example, Fu et al. [111] prepared a high-entropy carbon-coated NVPF cathode $Na_3V_{1.9}(Mg, Cr, Al, Mo, Nb)_{0.1}(PO_4)_2F_3$ (NVPF-HE@C), which consists of five different oxidation state ions doped at the V-site in order to improve the low-discharge platform with uniform distribution of the elements (Figure 16g). Interestingly, the NVPF-HE@C cathode exhibit higher D_{Na^+} values than NVPF@C in the high voltage region (3.7 V/4.2 V), suggesting faster apparent diffusion kinetics during redox reactions due to high entropy effects (Figure 16h).

Overall, V-site and PO_4^{3-}-site substitution have proven to be effective approaches for simultaneously regulating the electronic structure and Na^+ transport behavior of NASICON-type materials. Specifically, V-site substitution modifies the local electronic environment through the introduction of heterovalent metal ions, thereby enhancing electronic conductivity and optimizing the redox potential. In contrast, PO_4^{3-}-site substitution primarily tailors the structural framework and Na^+ migration pathways, leading to improved structural stability and ion diffusion kinetics. As a result, these modification strategies collectively contribute to enhanced specific capacity, energy density, and cycling durability of NVP-based cathodes. More importantly, they provide valuable insights into the structure property relationship and offer practical design principles for the development of advanced cathode materials for high-performance sodium-ion batteries.

6.4. Three-Site Co-Doping

Triple-site substitution, involving the simultaneous regulation of Na, V, and PO_4^{3-} sublattices, has emerged as an effective strategy for comprehensively optimizing NASICON cathodes. In this approach, Na-site substitution enlarges diffusion channels and facilitates Na^+ migration, while V-site substitution tailors the electronic structure, enhances charge-transfer kinetics, and improves redox activity. Concurrently, PO_4^{3-} site modification strengthens the polyanionic framework and further regulates the local coordination environment, contributing to enhanced structural stability. The synergistic interaction among these three substitution sites effectively reduces polarization, lowers ion-transport barriers, and suppresses structural degradation during prolonged cycling.

For instance, Sun et al. [112] synthesized $Na_{3.1-x}K_xV_{2-x}La_x(PO_4)_{2.9}(SiO_4)_{0.1}$ ($K/La_xSi_{0.1}$) cathode materials by sol-gel method to achieve ternary substitution including K, La and Si to replace the Na, V and PO_4^{3-} site, respectively (Figure 17a). The amount of introduced Si was limited to 0.1 to keep the structure undamaged. K^+ are responsible for the extension of the c axis, while the other two ions with larger ionic radii promote the extension of the crystal structure along the direction. Thus, they can improve the stability of the crystal backbone during Na^+ de-embedding by expanding the migration channels and reducing the resistance present in the neighboring coordination environments. The ternary substitution of $Na_3V_2(PO_4)_3$ by K^+, La^{3+}, and Si^{4+} reduces the band gap to 1.21 eV, which suggests that the dopants enhance electronic conductivity and improve the electrode reaction kinetics (Figure 17b). There is no doubt that the optimized KLS0.07 electrode possesses the best capacities of 117.4, 115.7, 111.5, 108.9, 103.8 and reversible 115.9 mAh g^{-1} at different rates of 0.3, 1, 2, 5, 10 and back to 1 C, respectively (Figure 17c).

The superior rate performance is attributed to the faster ionic pathway and the more robust crystal framework. In addition, the KLS0.07 composite has a high capacity of 109.3 mAh g^{-1} at a rate of 10 C with a capacity retention of 83.2% after 1500 cycles. At a rate of 50 C, the reversible capacity is 84.8 mAh g^{-1} with high capacity retention of 69.8% after 1300 cycles (Figure 17d). This is attributed to the fact that K still acts as a pillar in the crystal structure, and lanthanum and silicon take full advantage of their larger ionic radii to expand the crystal volume along the a/b direction. More importantly, the synergistic effect of multiple elements contributes to higher conductivity. Particularly in terms of kinetics, the fast diffusion ability of Na^+ ensures that the optimized opening structure can efficiently transport Na^+.

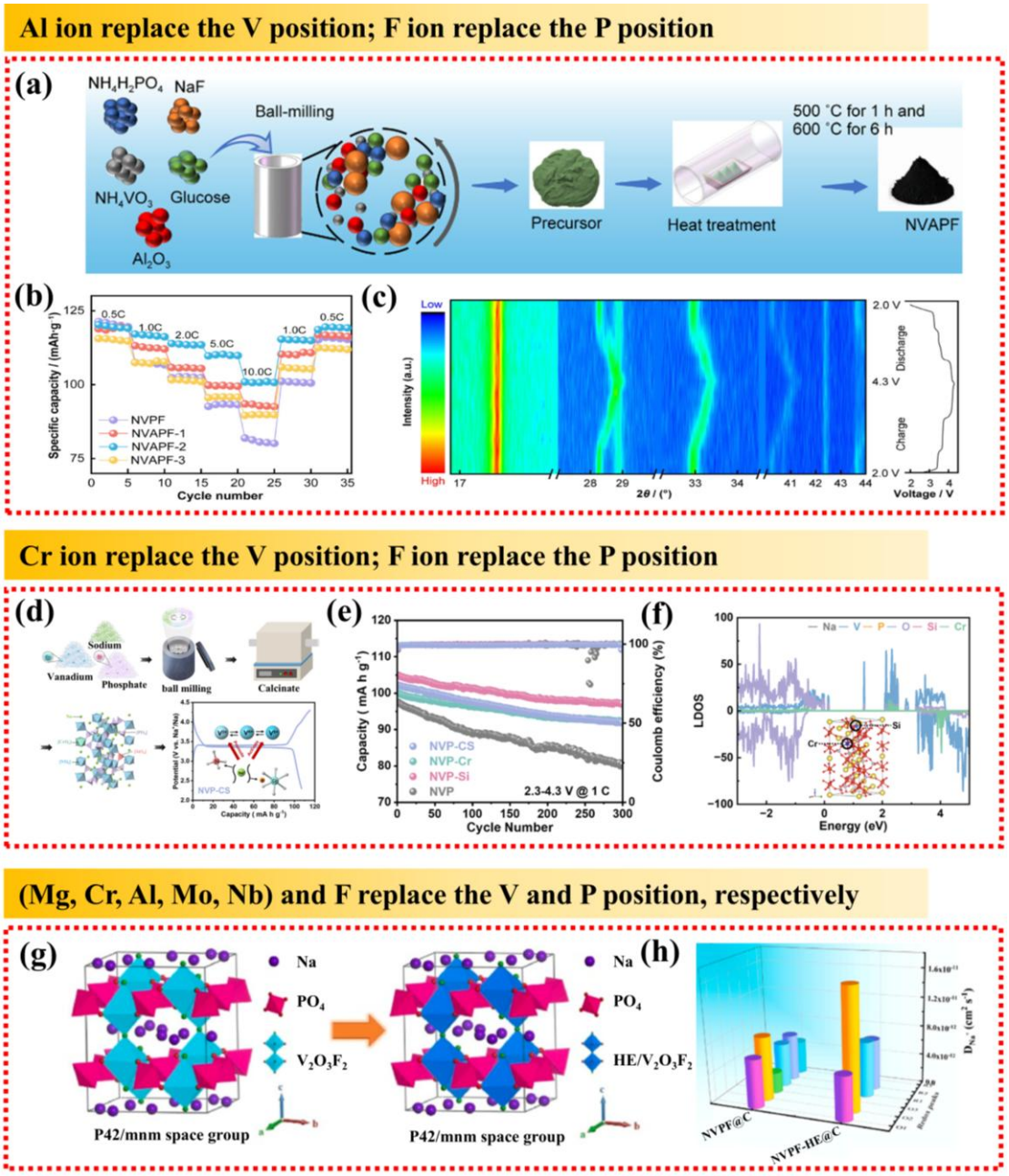

Figure 16. Examples of V site and PO_4^{3-} site co-doping: (**a**) Schematic illustrations for the synthesis process of $Na_3V_{2-x}Al_x(PO_4)_2F_3$. (**b**) Rate capability from 0.5 C to 10 C. (**c**) In-suit XRD patterns of NVAPF-2. Reproduced with permission from ref. [109]. Copyright 2024, The Non-ferrous Metals Society of China . (**d**) Schematic illustration of the synthesis of NVP-CS. (**e**) Cycling performance at 1 C. (**f**) Local density of states of NVP-CS. Reproduced with permission from ref. [110]. Copyright 2023, ACS. (**g**) Schematic illustration for the change of crystal structure from NVPF@C to NVPF-HE@C. (**h**) Na diffusion coefficients from CV. Reproduced with permission from ref. [111]. Copyright 2024, Elsevier.

Furthermore, Zhang et al. [113] synthesized K/Ni/F co-doped NVP composites ($Na_{2.96+x}K_{0.04}V_{2-x}Ni_x(PO_4)_{2.98}F_{0.06}$) via a sol-gel method. The introduction of K^+ enlarged Na^+ diffusion channels, while F substitution reduced particle size and shortened ion transport pathways (Figure 17e). Meanwhile, Ni^{2+} doping optimized the electronic structure and facilitated charge-transfer processes. In addition, carbon nanotube coating constructed an efficient conductive network, enhanced electronic conductivity, and alleviated structural deformation during cycling. Owing to the synergistic effects of triple-site substitution and conductive-network engineering, the optimized KNF@CNTs0.04 electrode delivered excellent rate capability, maintaining 86.1 mAh g^{-1} even at 100 C and recovering to 105.8 mAh g^{-1} when the current density returned to 1 C (Figure 17f). Moreover, its charge-transfer resistance was significantly reduced to 55 Ω, indicating accelerated reaction kinetics and enhanced structural stability (Figure 17g). These results demonstrate the effectiveness of combined K/Ni/F co-doping and CNT modification for developing high-performance NVP cathodes.

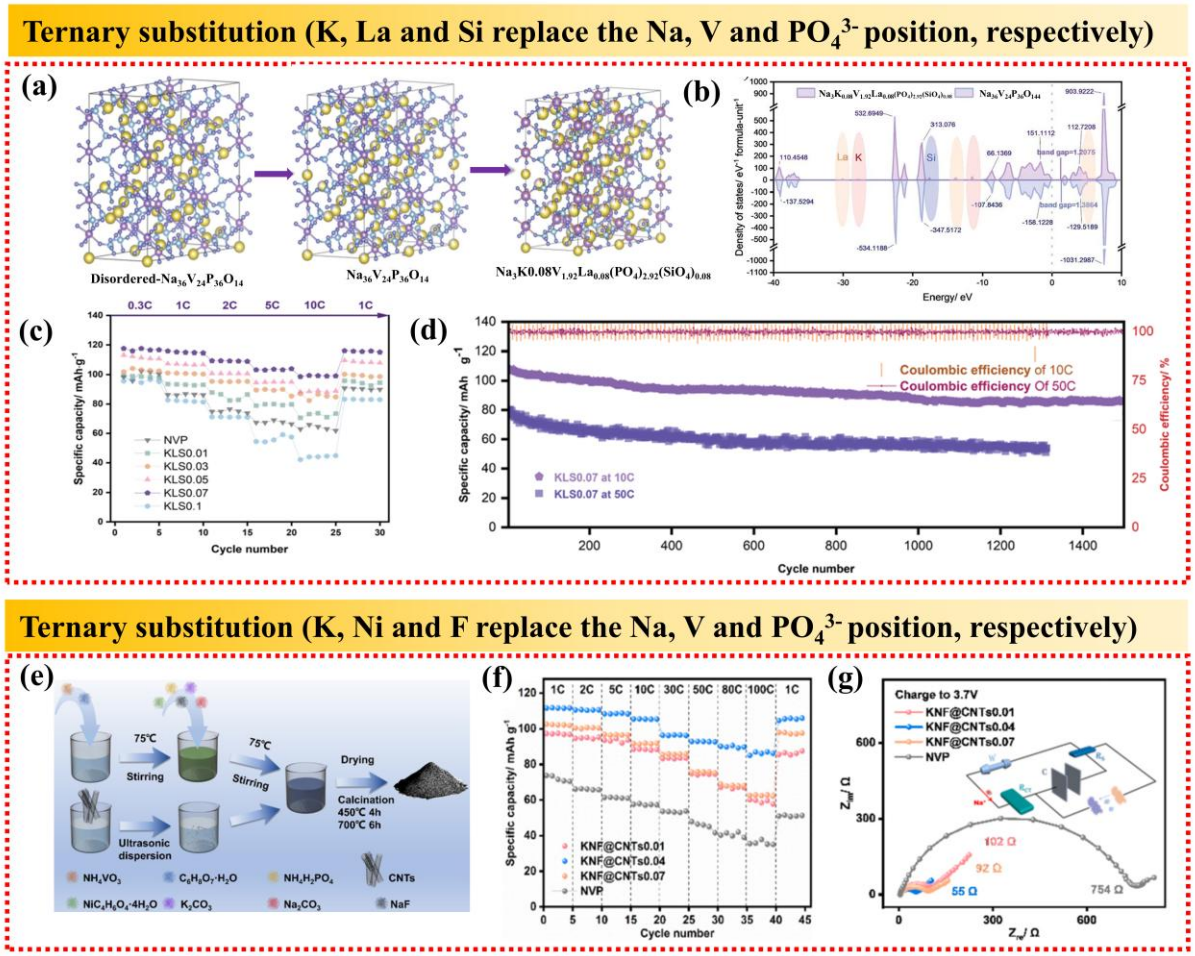

Figure 17. Examples of three site co-doping: (**a**) Diagram of lattice evolution of the samples. (**b**) The partial density of states of K_1-$Na_{35}La_1V_{23}Si_{35}O_{155}$ and $Na_{36}V_{24}P_{36}O_{144}$. (**c**) The rate performance of the samples. (**d**) Long cycling performance of KLS0.07 at 10 C and 50 C. Reproduced with permission from ref. [112]. Copyright 2022, RSC. (**e**) The flowchart of the synthesis of KNF@CNTs samples. (**f**) The rate performance for all samples. (**g**) Nyquist plots of the four electrode materials and their corresponding equivalent circuit models. Reproduced with permission from ref. [113]. Copyright 2024, Elsevier.

In a word, the three site substitution strategy provides a multi-dimensional regulatory pathway for the performance enhancement of NVP cathode materials. By precisely designing the transition metal sites (e.g., Ni^{2+} replaces V^{3+}), PO_4^{3-} sites (e.g., SiO_4^{4-}, F^- partially replaces PO_4^{3-}) and synergistic substitution of Na sites (e.g., K^+, Ca^{2+} doping) can significantly enhance the structural stability of NVPs, expand the Na^+ transport channels and improve the electronic conductivity. It is shown that this multisite synergy not only suppresses the phase transition and bulk strain during charging/discharging, but also accelerates the Na^+ diffusion kinetics by inducing charge redistribution through the introduction of heteroatoms. However, the optimization of atomic ratios for three sites substitution, the mechanism of interfacial side reactions during long cycling, and the scale-up preparation process still need to be further explored. In the future, combining theoretical calculations and advanced characterization

techniques to deeply resolve the interaction law between substitution sites will promote NVP-based cathode materials toward practical applications and help the industrialization of SIBs.

Compared with single-site substitution, multi-site co-doping offers synergistic effects that arise from the interplay among different sublattices, yielding performance enhancements that surpass the simple sum of individual modifications. These synergistic effects can be understood from three interrelated aspects. First, from a spatial perspective, Na-site doping (e.g., K^+) enlarges the lattice channels, while transition-metal-site doping (e.g., Zr^{4+}, Al^{3+}) reinforces the framework stability, their combination not only broadens Na^+ migration pathways but also prevents structural collapse during prolonged cycling, achieving a channel expansion plus structural reinforcement effect that cannot be realized by either single-site modification alone. Second, in terms of electronic structure, heterovalent ions at V-sites modulate the local density of states and narrow the bandgap, while anion-site substitution (e.g., F^-, SiO_4^{4-}) further alters the coordination environment around V and promotes more reversible redox reactions; this co-regulation of electronic structure and coordination environment lowers the Na^+ migration energy barrier beyond the effect of V-site doping alone. Third, from a kinetic viewpoint, the enlarged diffusion channels from Na-site substitution and the improved intrinsic electronic conductivity from V-site and anion-site substitution collectively reduce charge-transfer resistance and enhance ion/electron transport; this dual improvement in ionic and electronic conduction leads to substantially enhanced rate capability, with a multiplicative rather than additive effect on overall electrochemical performance. Based on these synergistic mechanisms, three general design principles for effective multi-site co-doping can be summarized: selecting dopants with complementary functions (e.g., pillar ions at Na-sites, redox-active ions at V-sites, and framework-stabilizing anions), precisely controlling doping ratios to avoid impurity phase formation, and ensuring that the combined lattice distortion remains within a tolerable range to maintain structural integrity. These principles provide practical guidance for the rational design of high-performance multi-site modified NVP cathodes.

7. Conclusions and Outlook

7.1. Conclusions

$Na_3V_2(PO_4)_3$ (NVP) has attracted extensive attention as a promising cathode material for sodium-ion batteries owing to its robust NASICON framework, high operating voltage, and excellent structural stability. However, its intrinsically low electronic conductivity, limited ion-transport kinetics, and the relatively high cost of vanadium remain major obstacles to practical application. In this review, recent advances in site-specific substitution engineering for NVP-based cathodes have been systematically summarized, including Na-site, V-site, PO4-site, and multi-site modification strategies. Among them, Na-site substitution primarily regulates lattice parameters and Na^+ migration pathways, thereby facilitating ion diffusion and improving rate capability. As is shown in Table 2, V-site engineering effectively tailors the electronic structure, introduces additional redox-active centers, and enhances both electronic conductivity and structural stability. Meanwhile, PO_4-site substitution modifies the local coordination environment and polyanionic framework, contributing to improved charge-transfer behavior, enhanced framework robustness, and accelerated Na^+ transport. More importantly, multi-site regulation integrates the advantages of individual substitution strategies and generates synergistic effects in both ionic and electronic transport, resulting in superior electrochemical performance. In recent years, medium-entropy and high-entropy engineering have further expanded the compositional design space of NVP materials by simultaneously optimizing structural stability, redox chemistry, and reaction kinetics through configurational entropy effects. Collectively, these studies demonstrate that rational site engineering is an effective approach for overcoming the intrinsic limitations of NVP and accelerating the development of high-performance sodium-ion battery cathodes.

7.2. Outlook

Despite the remarkable progress achieved in recent years, several critical challenges still need to be addressed before NVP-based cathodes can be widely commercialized.

First, although numerous dopants have been reported, the fundamental structure-property relationships governing site-specific substitution remain insufficiently understood. In many cases, performance enhancement is attributed to improved conductivity or Na^+ diffusion without quantitatively distinguishing the respective contributions of electronic structure modulation, lattice evolution, and defect chemistry. Advanced operando characterization techniques combined with first-principles calculations and machine-learning-assisted simulations are therefore required to establish a deeper mechanistic understanding of substitution-induced electrochemical behavior.

Table 2. The summary of the characteristics of transition metal doping.

Doping Type		Characteristic	Materials	Carbon Source	Carbon Content	Voltage Window	Rate Capability [mAh g^{-1}]	Cyclic Stability [mAh g^{-1}/cycle]	Ref.
Unit doping	Mn doping	Single-element doping at the V site can simultaneously activate new redox couples, facilitate Na^+ diffusion, and reinforce the lattice framework, yet it inevitably falls into the "trade-off dilemma" of performance compromise, owing to active-center dilution, Jahn–Teller instability, and a narrow compositional optimization window.	$Na_{3.75}Mn_{0.75}V_{1.25}(PO_4)_3$	VitC	~11.3 wt.%	2.5–4.2 V	105.6 (0.2 C)	78% (10 C/4000)	[75]
			$Na_3V_{1.5}Mn_{0.5}(PO_4)_3$	Citric Acid	~11 wt.%	1.4–4.0 V	170.9 (0.5 C)	91% (0.5C/100)	[76]
	Fe doping		$Na_{3.5}V_{1.5}Fe_{0.5}(PO_4)_3$	Oleic Acid	~12.5 wt.%	1.7–4.3 V	112 (0.5 C)	84% (100 C/10,000)	[77]
			$Na_{3.4}V_{1.7}Fe_{0.3}(PO_4)_3$	Citric Acid	-	1.8–4.2 V	176 (0.1 C)	64% (10 C/1000)	[78]
	Doping of other elements		$Na_3V_{4/3}Cr_{2/3}(PO_4)_3$@C	Citric Acid	~12.5 wt.%	1.5–4.4 V	94 (5000 mA g^{-1})	86% (5000 mA g^{-1}/2000)	[79]
			$Na_3V_{1.5}Al_{0.5}(PO_4)_3$	Citric Acid	~5.9 wt.%	1.0–4.4 V	142.6 (5 C)	87.9% (5 C/500)	[80]
			$Na_{2.5}V_{1.5}Ti_{0.5}(PO_4)_3$/C	Citric Acid	<3.5 wt.%	1.5–4.0 V	170.0 (50 mA g^{-1})	94.1% (1 A g^{-1}/1000)	[81]
			$Na_3V_{1.25}Ga_{0.75}(PO_4)_3$	Citric Acid	~7.74 wt.%	1.4–4.2 V	109.3 (0.5 C)	92.3% (1 C/400)	[82]
Multiple transition metals doping	Binary groups	Multi-element doping progressively enhances redox activity, ion transport, and structural integrity through synergistic and entropy-stabilization effects, yet it simultaneously introduces trade-offs in active-site dilution, lattice disorder, compositional sensitivity, and synthesis complexity with the balance shifting as the system evolves from binary to medium-entropy and ultimately to high-entropy configurations.	$Na_{3.83}V_{1.17}Mn_{0.58}Ni_{0.25}$ $(PO_4)_3$	Citric Acid	-	2.0–4.0 V	107.9 (0.2 C)	63.5% (20 C/10,000)	[83]
			$Na_{3.95}MnV_{0.95}Zr_{0.05}(PO_4)_3$/C	Citric Acid	~9.1 wt.%	2.5–3.8 V	95.4 (0.2 C)	83.1% (30 C/1000)	[84]
	Medium-entropy		$Na_{3.5}Fe_{0.5}VCr_{0.5}(PO_4)_3$/C	Citric Acid	~14.29 wt.%	1.8–4.5 V	148.2 (0.1 C)	95.1% (10 C/2000)	[85]
			$Na_{3.2}V_{1.7}(FeMnCo)_{0.1}(PO_4)_3$	Melamine and CNTs	-	2.0–4.5 V	121.7 (1 C)	77.7% (20 C/6000)	[86]
			$Na_{3.2}V_{1.1}Ti_{0.2}Al_{0.2}Cr_{0.2}Mn_{0.2}Ni_{0.1}(PO_4)_3$	Citric Acid	~5.5 wt.%	2.5–4.4 V	81 (5 C)	81.3% (30 C/10,000)	[87]
	High-entropy doping		$Na_3V_{1.5}(CrMnFeMgAl)_{0.5}(PO_4)_3$@C	Citric Acid	~4.6 wt.%	2.5–4.3 V	117.2 (0.2 C)	94.4% (20 C/5000)	[88]
			$Na_{3.12}MnTi_{0.9}(VFeMgCrZr)_{0.02}(PO_4)_3$	Citric Acid	~10.03 wt.%	1.5–4.3 V	169.6 (0.1 C)	81.7% (5 C/1000)	[89]
			$Na_3V_{1.47}$(Fe, Al, Ga, Mg, $Mn)_{0.5}Mo_{0.01}Nb_{0.02}(PO_4)_3$	Citric Acid	~11.47 wt.%	2.2–4.3 V	130.2 (0.5 C)	86.5% (15 C/1000)	[90]
Vanadium-free positive electrode		Vanadium-free cathodes reduce cost and resource dependence while improving sustainability through the use of abundant transition metals. However, they generally exhibit lower operating voltages, poorer conductivity, and slower Na^+ transport kinetics.	$NaFePO_4$-350 °C	-	-	1.4-4.6V	113 (0.1 C)	75.4% (7 C/1000)	[92]
			$Na_3MnTi(PO_4)_3$/C	PVP	~29.71 wt.%	1.5-4.2V	186.2 (0.1 C)	63.7% (1 C/6000)	[93]
			$Na_3MnTi_{0.5}Zr_{0.5}(PO_4)_3$/C	Citric Acid	-	2.0-4.3V	71.0 (10 C)	78.8% (2 C/1000)	[94]
Anionic site doping		Anionic-site substitution effectively regulates the local electronic environment and polyanionic framework, enhancing structural stability, Na^+ diffusion kinetics, and charge-transfer behavior. However, excessive substitution may distort the crystal structure, alter phase stability.	$Na_{3.1}V_2(PO_4)_{2.9}(SiO_4)_{0.1}$/C@rGO	Citric Acid	-	2.3-4.1V	113.6 (0.1 C)	79.0% (1 C/1000)	[99]
			$Na_{3.2}V_2(PO_4)_{2.9}MoO_{4(0.10)}$	Citric Acid	-	2.4-4.3V	92 (20 C)	81.6% (20 C/500)	[100]
			HTS-NVPF	-	~1.86 wt.%	2.0-4.5V	114.7 (0.5 C)	84.2% (10 C/1000)	[101]
Multi-site doping	Na/V co-doping	Multi-site co-doping provides a powerful multi-dimensional platform to synergistically enhance structural stability, Na^+	$Na_{3.9}K_{0.1}FeV(PO_4)_3$@C	Citric Acid	~12.7 wt.%	2.0–3.8 V	109.85 (0.2 C)	91.7% (5 C/3000)	[105]

		diffusion, and electronic conductivity through cooperative modulation at Na, V, and polyanionic sites. However, its practical application hinges on precise control over elemental coexistence, doping stoichiometry, phase purity, synthesis consistency, interfacial compatibility, mechanistic clarity, and lattice distortion tolerance.	$Na_{3.3}K_{0.1}Ca_{0.1}VMn_{0.8}Zr_{0.2}(PO_4)_3$	Citric Acid	~9.65 wt.%	2.5–3.8 V	73 (15 C)	92.7% (10 C/3000)	[106]
	Na/PO_4 co-doping		$N_{0.92}K_{0.08}$VPF/C	Citric Acid	~2.7 wt.%	2.5–4.3 V	128.8 (0.2 C)	60.2% (10 C/5000)	[107]
			$Na_{3.24}K_{0.10}V_{2.01}(PO_4)_{2.94}(SiO_4)_{0.14}$	-	-	2.8–3.9 V	116.3 (0.5 C)	44% (20 C/10000)	[108]
	V/PO_4^{3-} co-doping		$Na_3V_{1.9}Al_{0.1}(PO_4)_2F_3$	Glucose	-	2.0–4.3 V	103 (10 C)	92.1% (10 C/500)	[109]
			$Na_3V_{1.9}Cr_{0.1}(PO_4)_{2.9}(SiO_4)_{0.1}$	Citric Acid	-	2.3–4.3 V	94.1 (5 C)	82.6% (1 C/300)	[110]
			$Na_3V_{1.9}$(Mg, Cr, Al, Mo, Nb)$_{0.1}(PO_4)_2F_3$	Oxalic Acid	-	2.5–4.3 V	128 (1 C)	83% (5 C/800)	[111]
	Three site co-doping		KLS0.07	Oxalic Acid	~1-1.5 wt.%	2.3–4.1 V	117.4 (0.3 C)	83.2% (10 C/1500)	[112]
			$Na_3K_{0.04}V_{1.96}Ni_{0.04}(PO_4)_{2.98}F_{0.06}$	Citric Acid and CNTs	~5.11 wt.%	2.5–4.1 V	111.5 (1 C)	-	[113]

Second, current studies mainly focus on single-site or limited dual-site substitutions, whereas the compositional design space of multi-site regulation remains largely unexplored. Future efforts should emphasize synergistic engineering among Na, transition-metal, and polyanionic sublattices to simultaneously optimize ionic transport, electronic conductivity, redox activity, and structural durability. In particular, rational multi-site design may provide an effective route for balancing energy density, power capability, and cycle life.

Third, high-entropy and medium-entropy strategies have emerged as promising approaches for enhancing both structural stability and reaction kinetics through multi-element synergistic effects. Nevertheless, the entropy-driven mechanisms responsible for lattice stabilization, Na^+ migration, and charge compensation are still not fully clarified. Further investigations into entropy-related local structural evolution and electronic redistribution will be essential for guiding the design of next-generation NASICON cathodes.

Finally, practical applications require more attention beyond half-cell performance. Future research should focus on reducing vanadium consumption, developing vanadium-free or low-vanadium NASICON systems, increasing tap density and electrode loading, optimizing electrolyte compatibility at high voltages, and validating performance in full-cell configurations under realistic operating conditions. From a broader perspective, integrating site-specific substitution, entropy engineering, artificial intelligence-assisted materials discovery, and scalable synthesis technologies is expected to accelerate the commercialization of NVP-based cathodes and promote the widespread deployment of sodium-ion batteries in large-scale energy-storage applications.

Author Contributions

X.L.: Writing—original draft, conceptualization, methodology, investigation, formal analysis, data curation, visualization; B.X.: Writing—original draft, methodology, visualization; Z.B.: Writing—review & editing, investigation, data curation; R.W.: Writing—review & editing, methodology; D.C.: Writing—review & editing, data curation; Q.Z.: Writing—review & editing, validation; Q.K.: Writing—review & editing, supervision, conceptualization, project administration, funding acquisition; L.Y.: Writing—review & editing, conceptualization, supervision, project administration, funding acquisition. All authors have read and agreed to the published version of the manuscript.

Funding

This work was supported by Zhejiang Provincial Natural Science Foundation of China (Grant No. LQN26E010008). Zhejiang Provincial Association of Science and Technology's Young Talent Support and Cultivation Program (ZJSKQT2026134). National College Student Innovation and Entrepreneurship Training Program (No. 202610356016).

Institutional Review Board Statement

Not applicable.

Informed Consent Statement

Not applicable.

Data Availability Statement

Data will be made available on request.

Conflicts of Interest

The authors declare no conflict of interest.

Use of AI and AI-Assisted Technologies

No AI tools were utilized for this paper.

References

1. Bai, X.; Jia, N.; Jin, Y.C.; et al. Potential analysis of in-situ hydrogen generation in narrow reservoir with alternating steam-oxygen injection. *Energy Rep.* **2026**, *15*, 108893.
2. Abdulkadir, A.; Singh, H.; Aluna, L.; et al. Algae-based biopolymers for next-generation energy storage and sustainable development goals. *Process Saf. Environ. Prot.* **2026**, *209*, 108479.
3. Filipowicz, P.; Dziuba, M.; Saletnik, B. Technological advances in energy storage: Environmental and cyber challenges, opportunities and threats: A review. *Sustainability* **2026**, *18*, 3230.
4. Jafarizadeh, H.; Yamini, E.; Zolfaghari, S.M.; et al. Navigating challenges in large-scale renewable energy storage: Barriers, solutions, and innovations. *Energy Rep.* **2024**, *12*, 2179–2192.
5. Chen, S.; Wu, G.; Jiang, H.; et al. External Li supply reshapes Li deficiency and lifetime limit of batteries. *Nature* **2025**, *638*, 676–683.
6. Mishra, M.; Kumar, M. Elevating energy storage: High-entropy materials take center stage. *J. Energy Storage* **2024**, *91*, 112186.
7. Qin, Z.; Ma, J.; Zhu, M.; et al. Advancements in energy storage technologies: Implications for sustainable energy strategy and electricity supply towards sustainable development goals. *Energy Strategy Rev.* **2025**, *59*, 101710.
8. Zhu, Q.; Cheng, L.; Sun, X.; et al. LiC6@Li as a promising substitution of Li metal counter electrode for low-temperature battery evaluation. *Adv. Mater.* **2025**, *37*, 2419041.
9. Xiao, D.; Xu, X.; Xu, Z. Circular economy and energy storage technologies: A comprehensive approach to reduce emission and promoting sustainable growth. *Energy Rep.* **2025**, *13*, 6596–6608.
10. Bayus, S.; Mccleeary, D.; Diaz-Elsayed, N. Navigating the future of energy storage: A data mining and raw material cost analysis of lithium-ion and emerging batteries. *Energy* **2026**, *344*, 139835.
11. Cao, H.; Mao, Y.; Wang, B.; et al. Meta-reinforcement learning for fast charging design of diverse lithium-ion batteries. *J. Energy Storage* **2026**, *154*, 121327.
12. Islam, M.; Mahbubul, I.; Jadin, M.; et al. Lead-acid and lithium-ion batteries for electric mobility applications: A comparative review of performance, economics, industry trends, and future outlook. *J. Energy Storage* **2026**, *155*, 121187.
13. Quintana, J.; Paredes-Rojas, J.; Vázquez-Medina, R.; et al. Temperature and voltage effects on the charge and health of lithium-ion battery modules in light electric vehicles. *Sci. Rep.* **2026**, *16*, 9408.
14. Wei, C.; Cai, Y.; Xu, J.; et al. Review on gas production patterns, flammability, and detection methods of hydrogen-containing flammable gases during thermal runaway process in lithium-ion batteries. *Energies* **2026**, *19*, 398.
15. Bhutia, P.; Grugeon, S.; El Mejdoubi, A.; et al. Safety aspects of sodium-ion batteries: Prospective analysis from first generation towards more advanced systems. *Batteries* **2024**, *10*, 370.
16. Cai, X.; Yue, Y.; Yi, Z.; et al. Challenges and industrial perspectives on the development of sodium ion batteries. *Nano Energy* **2024**, *129*, 110052.
17. Chen, J.; Adit, G.; Li, L.; et al. Optimization strategies toward functional sodium-ion batteries. *Energy Environ. Mater.* **2023**, *6*, e12633.
18. Finsterle, T.; Kasper, J.; Knap, V.; et al. Suitability of sodium-ion-based battery pack as a cold-start alternative to a conventional 12 V/15 Ah lead-acid starter battery. *Monatsh. Chem.* **2026**, *157*, 887–896.
19. Gui, Q.; Xu, B.; Yu, K.; et al. Comparison of $NaNi_{1/3}Fe_{1/3}Mn_{1/3}O_2$ and $Na_4Fe_3(PO_4)_2(P_2O_7)$ cathode sodium-ion battery behavior under overcharging induced thermal runaway. *Chem. Eng. J.* **2024**, *497*, 154732.
20. Huang, X.; Jing, H.; Yang, M.; et al. Comparative study on thermal and gas characteristics of 26,700 sodium-ion and lithium-ion batteries. *J. Power Sources* **2025**, *631*, 236270.
21. Sandri, C.; Di Rienzo, R.; Deiaco, A.; et al. Sodium-ion batteries: A review of modeling, safety, and state estimation techniques. *J. Energy Storage* **2026**, *163*, 122120.
22. Tan, S.; Yang, H.; Zhang, Z.; et al. The progress of hard carbon as an anode material in sodium-ion batteries. *Molecules* **2023**, *28*, 3134.
23. Wan, X.; Li, Y.; Chen, S.; et al. Cathode modification of sodium-ion batteries for improved energy density: A review. *Adv. Sustain. Syst.* **2024**, *8*, 2400229.
24. Zhang, J.; Wu, T.; Zhao, X.; et al. Improvement of cycling stability of cathode materials and industrialization process for sodium-ion batteries. *J. Inorg. Mater.* **2025**, *40*, 348–362.
25. Zhang, L.; Huang, S.; Ding, Y.; et al. Research progress in the preparation of sodium-ion battery anode materials using ball milling. *RSC Adv.* **2025**, *15*, 6324–6341.
26. Zhao, W.; Wang, M.; Lin, H.; et al. Research progress on electrolyte key salts for sodium-ion batteries. *Prog. Nat. Sci. Mater. Int.* **2024**, *34*, 263–273.
27. Wang, L.; Tian, H.; Yao, X.; et al. Research progress and modification measures of anode and cathode materials for sodium-ion batteries. *ChemElectroChem* **2024**, *11*, e202300414.

28. Gu, Z.; Zhao, X.; Li, K.; et al. Homeostatic solid solution reaction in phosphate cathode: Breaking high-voltage barrier to achieve high energy density and long life of sodium-ion batteries. *Adv. Mater.* **2024**, *36*, 2400690.
29. Hao, Z.; Shi, X.; Zhu, W.; et al. Boosting multielectron reaction stability of sodium vanadium phosphate by high-entropy substitution. *ACS Nano* **2024**, *18*, 9354–9364.
30. Hu, J.; Li, X.; Liang, Q.; et al. Optimization strategies of $Na_3V_2(PO_4)_3$ cathode materials for sodium-ion batteries. *Nano-Micro Lett.* **2025**, *17*, 33.
31. Hu, Q.; Sun, M.; Zha, Y.; et al. Ti substitution strategy improves electrochemical performance of $Na_3V_2(PO_4)_2F_3$ cathode. *ACS Energy Lett.* **2025**, *10*, 1840–1850.
32. Jian, Q.; Gao, T.; Yang, W.; et al. Stabilizing the solid-solution sodium storage in Cr-substituted $Na_3V_2(PO_4)_3$ cathode for aqueous sodium-ion batteries with long-term stability. *J. Energy Chem.* **2025**, *105*, 797–805.
33. Kate, R.S.; Jadhav, H.S.; Chothe, U.P.; et al. Critical review of the recent progress and challenges of polyanion $Na_3V_2(PO_4)_3$ cathode materials in rechargeable sodium-ion batteries. *J. Mater. Chem. A* **2024**, *12*, 7418–7451.
34. Liao, X.; Wu, X.; Xie, M.; et al. Leveraging high-entropy substitution to achieve V^{4+}/V^{5+} redox couple and superior Na^+ storage in $Na_3V_2(PO_4)_3$-based cathodes for sodium-ion battery. *Energy Storage Mater.* **2025**, *77*, 104166.
35. Wang, A.; Liu, Y.; Yang, B.; et al. Bonding between vanadium and citric acid in solution affects the morphology of NVP/C and Na-ions storage performance. *J. Energy Storage* **2024**, *90*, 111835.
36. Wang, B.; Li, S.; Tian, Z.; et al. Anti-site defect regulation promoting V activity to induce brand new sodium storage sites for Na-rich type $Na_{3+2x}V_{2-x}Na_x(PO_4)_3$ with advanced performance. *Energy Storage Mater.* **2025**, *78*, 104278.
37. Yang, T.; Wu, Z.; Xu, X.; et al. Cation-anion Co-doped $Na_3V_2(PO_4)_3$ cathode for robust and high-performance sodium-ion storage. *Small Methods* **2026**, *10*, 2500370.
38. Zhou, Y.; Xu, G.; Lin, J.; et al. A multicationic-substituted configurational entropy-enabled NASICON cathode for high-power sodium-ion batteries. *Nano Energy* **2024**, *128*, 109812.
39. Liu, S.; Yan, X.; Cong, J.; et al. N-doped carbon decorated $Na_3V_2(PO_4)_3$@NC composite derived from melamine as cathode material for high-rate and ultralong-life sodium-ion batteries. *J. Solid State Chem.* **2024**, *335*, 124695.
40. Liu, Y.; Ullah, M.; Gao, X.; et al. Hierarchical fragmented $Na_3V_2(PO_4)_3$@reduced graphene composites with enhanced sodium-ion storage performance. *J. Power Sources* **2025**, *631*, 236230.
41. Ragul, S.; Prabakaran, A.; Sujithkrishnan, E.; et al. Sodium-ion battery using a NASICON-type $Na_3V_2(PO_4)_3$ cathode: Quantification of diffusive and capacitive Na^+ charge storage. *New J. Chem.* **2024**, *48*, 12323–12335.
42. Wang, Y.; Song, H.; Chai, S. Reduced graphene oxide-supported $Na_3V_2(PO_4)_3$/C cathode material synthesized by sol-gel method to improve electrochemical performances of sodium-ion batteries. *Int. J. Electrochem. Sci.* **2024**, *19*, 100773.
43. Xie, J.; Deng, X.; Lv, X.; et al. In_2O_3-induced $Na_3V_2(PO_4)_3$ nanosized growth for enhanced $Na_3V_2(PO_4)_3$/C electrochemical properties. *J. Energy Storage* **2026**, *142*, 119551.
44. Yang, Y.; Xu, G.-R.; Tang, A.-P.; et al. $Na_3V_2(PO_4)_3$-decorated $Na_3V_2(PO_4)_2F_3$ as a high-rate and cycle-stable cathode material for sodium ion batteries. *RSC Adv.* **2024**, *14*, 11862–11871.
45. Chen, J.; Liu, P.; Xu, K.; et al. Achieving long-term cycling stability in $Na_3V_2(PO_4)_3$ cathode material through polymorphic carbon network coating. *Carbon* **2025**, *238*, 120146.
46. Hu, J.; Chen, Z.; Ye, W.; et al. High-capacity NASICON-Type $Na_3V_{1.8}Cr_{0.2}(PO_4)_3$ cathode for high-performance sodium-ion batteries. *ACS Appl. Mater. Interfaces* **2025**, *17*, 45752–45763.
47. Ji, F.; Chen, K.; Chen, Z.; et al. Synergistic $Na_3V_2(PO_4)_3$-$Na_4Fe_3(PO_4)_2P_2O_7$ heterostructure cathode for superior-rate and ultrastable sodium storage. *Energy Storage Mater.* **2026**, *89*, 105144.
48. Li, Y.; Lai, X.; Yang, S.; et al. Unraveling the function mechanism of N-doped carbon-encapsulated $Na_3V_2(PO_4)_3$ cathode toward high-performance sodium-ion battery with ultrahigh cycling stability. *ACS Appl. Mater. Interfaces* **2025**, *17*, 3840–3851.
49. Li, Z.; Di, Y.; Song, W.; et al. Tailored synthesis of high-performance $Na_3V_2(PO_4)_3$ for Na-ion batteries through the sol-gel process. *ACS Appl. Energy Mater.* **2024**, *7*, 9551–9557.
50. Mo, Q.; Liang, Y.; Xu, W.; et al. $Na_3V_2(PO_4)_3$ anchoring on carbon spheres with promoted electrical conductivity and electrochemical performance in Zn-ion storage. *ECS J. Solid State Sci. Technol.* **2026**, *15*, 041002.
51. Wan, J.; Yang, X.; Xia, T. Preparation of Nb^{5+} doped $Na_3V_2(PO_4)_3$ cathode material for sodium ion batteries. *Materials* **2024**, *17*, 2697.
52. Yan, W.; Wang, X.; Han, Y.; et al. Green large-scale preparation of $Na_3V_2(PO_4)_3$ with good rate capability and long cycling lifespan for sodium-ion batteries. *ACS Sustain. Chem. Eng.* **2024**, *12*, 2394–2403.
53. Birusew, D.; Ledwaba, K.; Raphulu, M.; et al. Sodium vanadium phosphate cathodes for Na-ion batteries: Carbon modification strategies and electrolyte compatibility. *J. Energy Storage* **2026**, *150*, 120253.
54. Kate, R.; Chothe, U.; Deokate, R.; et al. High-performance $Na_3V_2(PO_4)_3$-based asymmetric sodium-ion full cells: Progress, strategies, and future outlook. *J. Power Sources* **2026**, *665*, 239010.

55. Wang, Z.; Li, Z.; Du, Z.; et al. $Na_3V_2(PO_4)_3$ cathode materials for advanced sodium-ion batteries: Modification strategies and density functional theory calculations. *J. Colloid Interface Sci.* **2025**, *682*, 760–783.
56. Zhang, R.; Hu, Y.; Li, J.; et al. In situ constructing ultrafast ion channel for promoting high-rate cycle stability of nano-$Na_3V_2(PO_4)_3$ cathode. *ACS Appl. Mater. Interfaces* **2024**, *16*, 2389–2396.
57. Zhang, S.; Zhou, T.; Pan, Y.; et al. Ternary $Na_3V_2(PO_4)_3/Na_3V_2(PO_4)_2F_3/NaV(P_2O_7)$ heterogeneous structure with interactive built-in electric field enables advanced sodium storage performance. *Adv. Funct. Mater.* **2026**, *36*, e11984.
58. Ju, Z.; Fu, W.; Wang, B.; et al. MOF-derived nickel-cobalt bimetallic sulfide microspheres coated by carbon: Preparation and long cycling performance for sodium storage. *Chin. J. Inorg. Chem.* **2025**, *41*, 661–674.
59. Xu, M.; Yang, Z.; Yuan, L.; et al. "Stepwise coating-thermolysis shrinkage" strategy for constructing yolk-shell bismuth/carbon composites enable outstanding stability for sodium ion battery. *J. Energy Chem.* **2026**, *118*, 201–210.
60. Wang, X.; Chu, Y.; Liu, S.; et al. Synergistic molecular modulation of π-π stacking for high-performance pitch-derived hard carbon anodes. *Energy Environ. Mater.* **2026**, e70444. https://doi.org/10.1002/eem2.70444.
61. Cong, J.; Luo, S.H.; Li, P.; et al. Ultracapacity properties of the refined structure in Na-rich $Na_{3.4}V_2(PO_4)_3$/C as sodium-ion battery cathodes by tapping the Na-vacancy Potential. *ACS Sustain. Chem. Eng.* **2023**, *11*, 16341–16353.
62. He, F.; Kang, J.; Liu, T.; et al. Research progress on electrochemical properties of $Na_3V_2(PO_4)_3$ as cathode material for sodium-ion batteries. *Ind. Eng. Chem. Res.* **2023**, *62*, 3444–3464.
63. Cong, J.; Luo, S.H.; Li, P.Y.; et al. Stable cycling performance of lituium-doping $Na_{3-x}LixV_2(PO_4)_3$/C ($0 \le x \le 0.4$) cathode materials by Na-site manipulation strategy. *Appl. Surf. Sci.* **2024**, *643*, 158646.
64. Shen, X.; Han, M.; Su, Y.F.; et al. Alkali metal ion induced lattice regulation for all climate NASICON-type cathode with superior Na-storage performance. *Nano Energy* **2023**, *114*, 108640.
65. Shen, L.; Li, Y.; Hu, C.; et al. A high-rate cathode material based on potassium-doped $Na_3V_2(PO_4)_3$ for high/low-temperature sodium-ion batteries. *Mater. Today Chem.* **2023**, *30*, 101506.
66. Mu, D.; Ma, J.; Gao, Y.; et al. Transition metals enhance the stability of the sodium vanadyl phosphate film in aqueous sodium-ion batteries. *J. Power Sources* **2026**, *682*, 240320.
67. Xu, S.; Chen, H.; Zhang, X.; et al. NASICON-type $NaTi_2(PO_4)_3$ surface modified O_3-type $NaNi_{0.3}Fe_{0.2}Mn_{0.5}O_2$ for high-performance cathode material for sodium-ion batteries. *ACS Appl. Mater. Interfaces* **2023**, *15*, 47764–47778.
68. Zhu, Y.; Li, W.; Chen, Y.; et al. Recent progress and prospects of manganese-based NASICON-type cathodes for Na-ion batteries. *Chem. Eng. J.* **2026**, *528,* 172272.
69. Soundharrajan, V.; Kim, S.; Nithiananth, S.; et al. Cathode nanoarchitectonics with $Na_3VFe_{0.5}Ti_{0.5}(PO_4)_3$: Overcoming the energy barriers of multielectron reactions for sodium-ion batteries. *Carbon Energy* **2024**, *6*, e551.
70. Soundharrajan, V.; Alfaza, G.; Arifiadi, A.; et al. $Na_{3.5}(MnVFeTi)_{0.5}(PO_4)_3$: A multi-transition-metal-ion-engineered NASICON-type cathodes for sodium ion batteries. *Batter. Supercaps* **2025**, *8*, e202400526.
71. Fan, Y.; Peng, Z.; He, J.; et al. Simultaneous modification of Na plus -rich and Mn^{2+}-doping on $Na_3V_2(PO_4)_3$ for superior electrochemical performance: Experimental and theoretical study. *J. Alloys Compd.* **2025**, *1010*, 177407.
72. Jiang, C.; Yu, Q.; Ding, Y. Enabling high working voltage and rate capability of NASICON cathode via moderately regulating coordination environment. *J. Energy Storage* **2025**, *119*, 116398.
73. Qian, C.; Shi, M.; Fan, C.; et al. Facile Al_2O_3 coating suppress dissolution of Mn^{2+} in Mn-substituted $Na_3V_2(PO_4)_3$ with outstanding electrochemical performance for full sodium ion batteries. *J. Colloid Interface Sci.* **2024**, *664*, 573–587.
74. Wang, B.; Zhao, Y.; Liu, S.; et al. Regulating the electronic and crystal structure of $Na_3V_2(PO_4)_3$ by pillar ionic substitution and p-type doping effects. *J. Energy Storage* **2024**, *99*, 113305.
75. Zhao, L.Z.; Wang, J.H.; Zhou, J.; et al. Rationally designed NASICON-type $Na_{3.75}V_{1.25}Mn_{0.75}(PO_4)_3$ cathode towards long life-span sodium ion batteries. *J. Electroanal. Chem.* **2023**, *941,* 117533.
76. Chen, Y.X.; Li, Q.P.; Wang, P.; et al. High-energy-density cathode achieved via the activation of a three-electron reaction in sodium manganese vanadium phosphate for sodium-ion batteries. *Small* **2023**, *19*, 2304002.
77. Zhou, Y.F.; Xu, G.F.; Lin, J.D.; et al. Reversible multielectron redox chemistry in a NASICON-type cathode toward high-energy-density and long-life sodium-ion full Batteries. *Adv. Mater.* **2023**, *35*, 2304428.
78. Bai, Z.C.; Wang, R.; Zong, Q.; et al. Kinetically accelerated sodium storage in $Na_3V_{1.7}Fe_{0.3}(PO_4)_3$ enabled by activation of V^{4+}/V^{5+} redox couples, oxygen vacancies and carbon composite engineering. *Chem. Eng. J.* **2025**, *523*, 168804.
79. Mai, B.; Xing, B.Y.; Yue, Y.F.; et al. Cr-doped $Na_3V_2(PO_4)_3$@C enables high-capacity with V^{2+}/V^{5+} reaction and stable sodium storage. *J. Mater. Sci. Technol.* **2023**, *165*, 1–7.
80. Sun, C.; Zhao, Y.J.; Ni, Q.; et al. Reversible multielectron redox in NASICON cathode with high energy density for low-temperature sodium-ion batteries. *Energy Storage Mater.* **2022**, *49*, 291–298.
81. Zhu, L.; Wang, M.M.; Xiang, S.; et al. Exceeding three-electron reactions in polyanionic cathode to achieve high-energy density for sodium-ion batteries. *ACS Nano* **2024**, *18*, 13073–13083.
82. Chen, Y.; Liao, X.; Wang, P.; et al. A high-energy-density NASICON-type $Na_3V_{1.25}Ga_{0.75}(PO_4)_3$ cathode with reversible V^{4+}/V^{5+} redox for sodium ion batteries. *J. Colloid Interface Sci.* **2024**, *653*, 1–10.

83. Chen, R.Y.; Zhang, X.Y.; Li, D.D.; et al. Novel NASICON-Type Na-V-Mn-Ni-containing cathodes for high-rate and long-life SIBs. *Small* **2024**, *20*, 2306589.
84. Wang, L.; Wang, J.Q.; Wang, L.L.; et al. Synergistic strain suppressing and interface engineering in $Na_4MnV(PO_4)_3$/C for wide-temperature and long-calendar-life sodium-ion storage. *ACS Nano* **2024**, *18*, 10863–10873.
85. Li, H.; Wang, Y.; Zhao, X.D.; et al. A multielectron-reaction and low-strain $Na_{3.5}Fe_{0.5}VCr_{0.5}(PO_4)_3$ cathode for Na-ion batteries. *ACS Energy Lett.* **2023**, *8*, 3666–3675.
86. Sun, S.; Liu, S.; Chen, Y.; et al. Quantum physics and deep learning to reveal multiple dimensional modified regulation by ternary substitution of iron, manganese, and cobalt on $Na_3V_2(PO_4)_3$for superior sodium storage. *Adv. Funct. Mater.* **2023**, *33*, 2213711.
87. Wu, X.H.; Jiang, W.J.; Dai, C.; et al. A phase-transition-free sodium vanadium phosphate cathode via medium-entropy engineering for superior sodium ion batteries. *Adv. Mater.* **2025**, *37*, 2414358.
88. Wang, S.Y.; Xu, T.D.; Leng, H.T.; et al. Synergetic effects from a high-entropy NASICON-type cathode for advanced sodium-ion batteries. *J. Mater. Chem. A* **2024**, *12*, 33617–33623.
89. Zhang, N.; Dong, X.R.; Yan, Q.; et al. High-entropy doping NASICON-Cathode breaks the kinetic barriers and suppresses voltage hysteresis for sodium ion batteries. *Energy Storage Mater.* **2024**, *72*, 103734.
90. Liao, X.Y.; Li, Y.J.; Xie, B.; et al. Unlocking advanced sodium storage performance: High-entropy modulates crystallographic sites with reversible multi-electron reaction. *Energy Storage Mater.* **2025**, *74*, 103920.
91. Liu, X.; Zhu, C.; Xu, T.; et al. Multifunctional-element doping of NASICON-structured cathode enables high-rate and stable sodium storage. *Chem. Eng. J.* **2024**, *497*, 154304.
92. Lu, X.; Liu, X.; Li, Y.; et al. Easy approach of highly electrochemical-active maricite $NaFePO_4$ cathode for low cost and high rate sodium-ion batteries. *Appl. Phys. Lett.* **2023**, *123*, 043903.
93. Ren, W.; Wang, Y.Y.; Hu, X.P.; et al. Electrospun $Na_3MnTi(PO_4)_3$/C film: A multielectron-reaction and free-standing cathode for sodium-ion batteries. *Chem. Eng. J.* **2024**, *487*, 150492.
94. Rao, K.; Sui, Y.; Deng, M.; et al. A novel NASICON-type $Na_3MnTi_{0.5}Zr_{0.5}(PO_4)_3$ cathode material with multivalent redox reaction for high performance sodium-ion batteries. *J. Colloid Interface Sci.* **2025**, *678*, 359–368.
95. Kong, W.; Yang, W.; Ning, D.; et al. Tuning anionic/cationic redox chemistry in a P2-type $Na_{0.67}Mn_{0.5}Fe_{0.5}O_2$ cathode material via a synergic strategy. *Sci. China Mater.* **2020**, *63*, 1703–1718.
96. Liu, M.; Li, M.; Zhang, B.; et al. Anionic group doping of $Na_4Fe_3(PO_4)_2P_2O_7$ stabilizes its structure and improves electrochemical performance for sodium ion storage. *ACS Sustain. Chem. Eng.* **2023**, *11*, 18102–18111.
97. Wang, L.; Cai, S.; Wang, D.; et al. Synergistic cationic-anionic regulation in Ni-Doped FeSe@C anodes with Se vacancies for high-efficiency sodium storage. *Batteries* **2025**, *11*, 205.
98. Wen, B.; Xiao, J.; Miao, Y.; et al. Selenium-induced anion vacancy and active site migration stimulating remarkable sulfide Na-ion storage. *J. Colloid Interface Sci.* **2024**, *675*, 980–988.
99. Chen, Y.; Cheng, J.; He, Z.; et al. Silicon substituted $Na_3V_2(PO_4)_3$/C nanocomposites enwrapped on conducting graphene for high-rate and long-lifespan sodium ion batteries. *Ceram. Int.* **2020**, *46*, 27660–27669.
100. Liu, X.; Gong, J.; Wei, X.; et al. MoO_4^{2-}-mediated engineering of $Na_3V_2(PO_4)_3$ as advanced cathode materials for sodium-ion batteries. *J. Colloid Interface Sci.* **2022**, *606*, 1897–1905.
101. Song, Z.; Liu, Y.; Guo, Z.; et al. Ultrafast synthesis of large-sized and conductive $Na_3V_2(PO_4)_2F_3$ simultaneously approaches high tap density, rate and cycling capability. *Adv. Funct. Mater.* **2024**, *34*, 2313998.
102. Wu, L.; Zhang, Y.; Wu, Z.; et al. Stabilized O_3-Type layered sodium oxides with enhanced rate performance and cycling stability by dual-site Ti^{4+}/K^+ substitution. *Adv. Sci.* **2023**, *10*, 2304067.
103. Yu, F.; He, Y.; He, Y.; et al. Stabilizing the structure and enhancing the kinetics of O_3-type layered cathodes for high-performance sodium-ion batteries via targeted multi-element synergistic doping. *Small* **2026**, *22*, e73623.
104. Xie, M.; Chen, Y.; Lin, D.; et al. Synergistic gallium and silicon co-doping for high-performance NASICON-type cathodes for sodium-ion batteries. *J. Energy Storage* **2026**, *166*, 122405.
105. Zhou, J.; Zhang, W.; Bai, J.; et al. Potassium-pillared $Na_4FeV(PO_4)_3$@C cathode for high-performance sodium-ion batteries. *Electrochem. Commun.* **2025**, *173,* 107883.
106. Chen, C.; Wang, L.; Deng, Z.; et al. Enabling one-step de-sodiation of $Na_4MnV(PO_4)_3$ cathode via regulating coordination environment for high-power and long-lasting sodium-ion batteries. *Adv. Funct. Mater.* **2025**, *35*, 2418642.
107. Wu, Q.; Ma, Y.; Zhang, S.; et al. Achieving a rapid Na^+ migration and highly reversible phase transition of NASICON for sodium-ion batteries with suppressed voltage hysteresis and ultralong lifespan. *Small* **2024**, *20*, 2404660.
108. Dou, M.; Zhang, Y.; Wang, J.; et al. Simultaneous cation-anion regulation of sodium vanadium phosphate cathode materials for high-energy and cycle-stable sodium-ion batteries. *J. Power Sources* **2023**, *560*, 232709.
109. Wang, S.-M.; Li, J.-Q.; Xu, L.; et al. Manipulation of $Na_3V_2(PO_4)_2F_3$ via aluminum doping to alter local electron states toward an advanced cathode for sodium-ion batteries. *Rare Met.* **2024**, *43*, 4253–4262.

110. Li, P.; Gao, M.; Wang, D.; et al. Optimizing vanadium redox reaction in $Na_3V_2(PO_4)_3$ cathodes for sodium-ion batteries by the synergistic effect of additional electrons from heteroatoms. *ACS Appl. Mater. Interfaces* **2023**, *15*, 9475–9485.
111. Fu, W.; Li, B.; Wang, P.; et al. A high-entropy carbon-coated $Na_3V_{1.9}(Mg, Cr, Al, Mo, Nb)_{0.1}(PO_4)_2F_3$ cathode for superior performance sodium-ion batteries. *Ceram. Int.* **2024**, *50*, 16166–16171.
112. Sun, S.; Chen, Y.; Bai, Q.; et al. Unraveling the modified regulation of ternary substitution on $Na_3V_2(PO_4)_3$ for sodium ion batteries. *J. Mater. Chem. A* **2022**, *10*, 11340–11353.
113. Zhang, J.; Zhang, B.; Chen, Y. Insights into the ternary substitution $Na_{2.96+x}K_{0.04}V_{2-x}Ni_x(PO_4)_{2.98}F_{0.06}$ with superior rate capability and near-zero strain property. *J. Energy Storage* **2024**, *102*, 114204.